# Chitosan/PLGA-based tissue engineered nerve grafts with SKP-SC-EVs enhance sciatic nerve regeneration in dogs through miR-30b-5p-mediated regulation of axon growth

Miaomei Yu [a,b,1], Mi Shen [a,1], Daiyue Chen [a], Yan Li [a], Qiang Zhou [a], Chunyan Deng [a], Xinyang Zhou [a], Qi Zhang [a], Qianru He [a], Hongkui Wang [a], Meng Cong [a], Haiyan Shi [a,c], Xiaosong Gu [a], Songlin Zhou [a,**], Fei Ding [a,*]

[a] *Key Laboratory of Neuroregeneration of Jiangsu and Ministry of Education, Co-Innovation Center of Neuroregeneration, NMPA Key Laboratory for Research and Evaluation of Tissue Engineering Technology Products, Nantong University, Nantong, Jiangsu, 226001, China*
[b] *Clinical Medical Research Center, The Third Affiliated Hospital of Soochow University, Changzhou, Jiangsu, 213003, China*
[c] *Department of Pathophysiology, School of Medicine, Nantong University, Nantong, Jiangsu, 226001, China*

## ARTICLE INFO

## ABSTRACT

Extracellular vesicles from skin-derived precursor Schwann cells (SKP-SC-EVs) promote neurite outgrowth in culture and enhance peripheral nerve regeneration in rats. This study aimed at expanding the application of SKP-SC-EVs in nerve grafting by creating a chitosan/PLGA-based, SKP-SC-EVs-containing tissue engineered nerve graft (TENG) to bridge a 40-mm long sciatic nerve defect in dogs. SKP-SC-EVs contained in TENGs significantly accelerated the recovery of hind limb motor and electrophysiological functions, supported the outgrowth and myelination of regenerated axons, and alleviated the denervation-induced atrophy of target muscles in dogs. To clarify the underlying molecular mechanism, we observed that SKP-SC-EVs were rich in a variety of miRNAs linked to the axon growth of neurons, and miR-30b-5p was the most important among others. We further noted that miR-30b-5p contained within SKP-SC-EVs exerted nerve regeneration-promoting effects by targeting the Sin3a/HDAC complex and activating the phosphorylation of ERK, STAT3 or CREB. Our findings suggested that SKP-SC-EVs-incorporating TENGs represent a novel type of bioactive material with potential application for peripheral nerve repair in the clinic.

## 1. Introduction

Peripheral nerve regeneration and functional recovery are still major clinical challenges [1]. The repair of peripheral nerve injury (PNI), especially in cases involving long-distance nerve defects, usually requires surgical nerve grafting, among which autografting, accepted as the gold standard, is unfortunately limited by several drawbacks, such as graft availability, donor site morbidity, neuroma formation and additional surgical incisions. Tissue engineered nerve grafts (TENGs) are developed by combining a nerve guidance conduit (NGC) with biochemical cues (support cells and/or bioactive factors) to serve as a promising alternative to nerve autografts [2].

Schwann cells (SCs) were first used as support cells due to their high neuroaffinity and unique neurotropic and neurotrophic functions [3]. Then, stem cells from different sources are gradually adopted to supplement or replace SCs for TENG applications in that stem cells can be induced to differentiate into SCs [4], thus accelerating axon growth and creating a favorable microenvironment for myelination [5]. Another explanation is that the positive effects of stem cell therapy are likely due to the paracrine activity of stem cells rather than their homing and differentiation in injured tissues [6].

Skin-derived precursors (SKPs), featured by their capacities of self-renewal and multipotent differentiation, have been considered as adult stem cell sources for regenerative therapies. Under specific culture

---

conditions, SKPs are induced to differentiate into SCs. Interestingly, SKP-derived SCs (SKP–SCs) were found to facilitate axon myelination and express myelin-related proteins when they are co-cultured with embryonic rat dorsal root ganglion (DRG) neurons *in vitro* [7]. Moreover, SKP-SCs can act as functional SCs to be introduced into artificial nerve grafts, which aid peripheral nerve regeneration [8–12].

As is known, extracellular vesicles (EVs) released by various cell types, including stem cells and precursors, play a crucial role in communication with recipient cells within the tissue microenvironment by transferring bioactive proteins, lipids and nucleic acids [13,14]. In previous studies, we showed that SKP-SC-EVs promoted axonal outgrowth and regeneration of motor neurons via Akt/mTOR/p70S6K pathway and improved neurite outgrowth of DRG sensory neurons by negatively regulating PTEN via miR-21-5p contained in EVs [15,16]. *In vivo*, we further inoculated SKP-SC-EVs into NGCs, either silicone tubes or chitosan conduits, to create artificial nerve grafts, which were applied to bridge 10- or 15-mm long sciatic nerve defects in rats. Our findings highlighted the feasibility of using SKP-SC-EVs for PNI repair in rats and contributed to exploring the potential clinical application of SKP-SC-EVs-containing TENGs [17]. However, whether SKP-SC-EVs contain other miRNAs, in addition to miR-21b-5p, that contribute to promoting neural growth remains unclear.

In order to accelerate the translation of SKP-SC-EVs-containing TENGs to the clinic, this study was designed to investigate the outcome of SKP-SC-EVs-based therapy in Beagle dogs. Canines represent a more suitable model for human studies than rats which had been used in our previous study [17,18]. To match the changes in experimental subjects, we first prepared a chitosan/poly (lactide-*co*-glycolide) (PLGA)-based NGC (Chinese Patent No. ZL 0110820.9), which had achieved considerable success in PNI repair [19], and then integrated SKP-SC-EVs into the NGC lumen, thus creating a TENG of novel configuration, which was applied to bridge a 40-mm long sciatic nerve defect in the Beagle dog. A combination of motor function, electrophysiological and histomorphological assessments were performed to evaluate the outcome of PNI repair, and the possible molecular mechanisms underlying the promotive effect of SKP-SC-EVs on peripheral nerve regeneration were preliminarily examined.

## 2. Materials and methods

### 2.1. Culture and identification of SKP-SCs

SKPs were isolated from the skin tissue of neonatal SD rats and induced to differentiate into SKP-SCs as described previously [16]. The acquired SKP-SCs were seeded on dishes coated with poly-D-lysine (Sigma-Aldrich, St. Louis, MO, USA) and laminin (Corning, Brooklyn, NY, USA) for culture in DMEM/F12 (3:1) medium supplemented with 3 % fetal bovine serum (Gibco, Carlsbad, CA, USA), 2 % N2 supplement (StemCell Technologies, Vancouver, BC, Canada), 5 μM forskolin (Sigma-Aldrich), 50 ng/ml heregulin-1β (R&D Systems, MN, USA), and 1 % penicillin/streptomycin (Beyotime, Shanghai, China).

After being fixed with 4 % paraformaldehyde and blocked for 1.5 h at room temperature, SKP-SCs were incubated with anti-GFAP (1:500, Abcam, Cambridge, MA, USA) and anti-S100 (1:500, Abcam) at 4 °C overnight, followed by reaction with Alexa Fluor 594-conjugated anti-mouse IgG and Alexa Fluor 488-conjugated anti-rabbit IgG secondary antibody (1:400, Abcam) at 37 °C for 2 h, and the cell nuclei were counterstained with a fluorescent blocking agent (Beyotime) containing 4′,6-diamidino-2-phenylindole (DAPI). Photomicrographs were taken under a confocal microscope (SP5, Leica, Mannheim, Germany).

### 2.2. Extraction and characterization of SKP-SC-EVs

SKP-SCs were inoculated in poly-D-lysine/laminin-coated dishes until the cell density reached 80 %. The original medium was discarded and cells were washed with pre-heated phosphate buffered saline (PBS),

followed by addition of the serum-free SKP-SCs medium. After 48 h culture, the supernatant was collected, centrifuged at 4 °C at 500 g for 10 min to remove cell debris, filtered at 0.22 μm syringe filter (Millipore, Billerica, MA, USA) and stored in a −80 °C refrigerator for later use.

SKP-SC-EVs in supernatants were isolated according to the instructions of the exoEasy Maxi Kit (Qiagen, Germantown, MD, USA). The concentration and particle size distribution of SKP-SC-EVs were measured by nanoparticle tracking analysis using a ZetaView (Particle Metrix, Ammersee, Germany), the morphology of SKP-SC-EVs was verified under a transmission electron microscope (Hitachi, Tokyo, Japan), and the EV-surface-specific markers were identified by Western blot analysis.

### 2.3. Animals and surgical procedure

A total of 15 male beagle dogs, aged 9 months and weighing 8.1–10.0 kg, were supplied by Yizheng Anlimao Biotechnology Co., Ltd. (Yangzhou, Jiangsu, China). Each animal was housed in a separate cage, and fed with standard dog food and water. Animals were anesthetized by intramuscular injection with compound anesthetics (1.4 ml/kg) before surgical procedures. The sciatic nerve in the left lateral thigh was exposed by making a skin incision and splitting the underlying muscles. A sciatic nerve segment was immediately transected and removed, leaving a 40-mm defect after retraction of the nerve stumps. All animals were randomly divided into 3 groups: autograft, TENG and EV-TENG groups. Surgical nerve grafting was applied to animals in 3 groups in a routine fashion: a nerve graft was implanted to bridge the sciatic nerve defect with both the proximal and distal nerve stumps being inserted ~1 mm into the graft's lumen (except for the autograft group) and then being sutured to the graft, followed by closure of the surgical incision (Fig. S1A).

In the autograft group, the nerve graft was just the removed nerve segment, and immediately re-implanted into the sciatic nerve defect. In the TENG group, the nerve graft was just a chitosan/PLGA-based NGC (Fig. S1B), which was prepared by inserting 3 bundles of longitudinally aligned PLGA fibers (42-mm long) into the lumen of a chitosan-based NGC (i.d. = 4 mm and length = 40 mm), as described previously [20] followed by injecting 500 μl of a 1:1 mixture of growth factor reduced (GFR) Matrigel (Corning, Brooklyn, NY, USA) and PBS. For the EV-TENG group, SKP-SC-EVs ($32 \times 10^{10}$ particles in 250 μl PBS) and GFR Matrigel were mixed at 1:1 ratio (by volume), and administered by injection into the lumen of the chitosan/PLGA-based NGC. Here the dose of SKP-SC-EVs was calculated mainly by referring to the repair effect for 10-mm long rat sciatic nerve defect as described in a previous study [17] and reconciling the volume of NGC lumen in this study. After grafting, the outcome of sciatic nerve repair in dogs was evaluated in a standardized and comprehensive way (Fig. S1C).

In addition, another set of experiments was performed on adult Sprague-dawley (SD) rats (male, weight about 200 g, n = 4), which were randomly divided into 2 groups. After deep anesthesia of rats by intraperitoneal injection with compound anesthetics (0.35 ml/100 g) containing 42.5 mg/ml chloral hydrate and 8.86 mg/ml pentobarbital sodium, the right sciatic nerve of rats in both groups was exposed, and then crushed for 30 s with toothless needle-holding forceps. A 10 μl mixture of miR-30b-5p agomir with GFR Matrigel (at a volume ratio of 1:1) and a 10 μl mixture of miR-negative control (NC) agomir with GFR Matrigel (at a volume ratio of 1:1) were respectively injected into 2-mm proximal to the crush site of rat sciatic nerve in 2 groups. On the 6th day post-surgery, the heart of rats was perfused sequentially with saline and 4 % paraformaldehyde, and the injured sciatic nerve of rats was harvested.

### 2.4. Gross observation and motor function test

All animals were housed and fed routinely post-surgery. The appearance, appetite, response and locomotive activities of dogs were

monitored. The gait and standing posture of dogs were recorded with video and photographs by 2 investigators blind to the treatment at 12 and 24 weeks post-surgery respectively. To evaluate the motor function of hind limbs quantitatively, the hind limb function score was determined by referring to an established scale [20], which involves postures, muscle atrophy, hind limb movement, hind limb force, stand upright and joint motion.

### 2.5. Electrophysiological evaluation

At 24 weeks post-surgery, animals were subjected to electrophysiological assessments as described previously [20]. Under deep anesthesia, the sciatic nerve on the injured side was re-exposed, electrical stimuli at 10 mA intensity were sequentially applied to the sciatic nerve trunk at the distal and proximal stumps of the injury site, and compound muscle action potentials (CMAPs) were recorded on the gastrocnemius (GC) belly on the ipsilateral side. The motor nerve conduction velocity (MNCV) value was calculated as a ratio of the distance between the proximal and distal stimulated sites to the CMAP latency difference. Normal CMAPs were measured on the contralateral, uninjured side.

### 2.6. Fluorogold retrograde tracing

Fluorogold (FG) retrograde tracing was performed to 3 dogs randomly selected from each group by injecting 100 µl of 5 % FG solution (Biotium, Hayward, CA, USA) into sciatic nerve trunk ~5 mm from the distal end of nerve graft and then suturing the incision. After survival for 2 weeks, dogs were transcardially perfused sequentially with saline and 4 % paraformaldehyde. The vertebral canal was opened before the lumbar spinal cord was exposed, and L6, L7 and S1 were excised together with the DRGs. After formaldehyde fixation and sucrose gradient dehydration (10, 20 and 30 % by weight), tissue samples were sectioned on a cryostat to obtain 30-µm-thick transverse sections for spinal cord and 20-µm-thick longitudinal sections for DRGs. The sections were counterstained with Hoechst 33258 (Beyotime) and viewed under a fluorescent microscope (Axio Imager M2, Zeiss, Oberkochen, Germany) with ultraviolet illumination, and micrographs were taken. The percentage of FG-positive sensory neurons in DRGs and the number of FG-positive motor neurons in spinal anterior horn were measured and analyzed by Image J software (NIH, Bethesda, MD, USA), respectively.

### 2.7. Transmission electron microscopic examination

Transmission electron microscopy (TEM) was used for morphological examination of extracted SKP-SC-EVs, which were ultrafiltered to a concentration of more than $10^{12}$ particles/ml and were loaded onto a formvar/carbon electron microscopy grid covered with an absorption membrane, followed by air-dry at room temperature for 20 min. After being washed and stained with 2 % phosphotungstic acid solution (Electron Microscopy Sciences, Washington, PA, USA), the grid was viewed under TEM (Jeol, Tokyo, Japan).

TEM was also applied to examine their morphological changes of animal tissues at 24 weeks post-surgery. Under deep anesthesia, the sciatic nerve or the GC muscle was freshly removed, followed by fixation in the pre-cooled fixative solution containing 4 % paraformaldehyde and 0.5 % glutaraldehyde. The nerve or muscle sample was immersed in pre-cooled glutaraldehyde and fixed with 1 % osmium tetraoxide solution. After wash, gradient ethanol dehydration, Epon 812 epoxy embedding and localization on semi-thin sections, the samples were cut into ultra-thin sections to undergo staining with lead citrate and uranyl acetate, followed by observation under TEM and morphometric analysis as described previously [20,21].

### 2.8. Histological assessment

At 24 weeks post-surgery, dogs were deeply anesthetized, and the tibialis anterior (TA) and GC muscles on the bilateral (injured and contralateral, uninjured) sides were excised and weighed immediately. The wet weight ratio of muscles was obtained by dividing the muscle mass on the injured side by that on the contralateral, uninjured side. The muscle samples were fixed with 4 % paraformaldehyde, dehydrated with gradient ethanol, embedded in paraffin, and cut into 5-µm-thick cross sections. Masson trichrome staining was performed according to the kit instructions (Solarbio, Beijing, China), followed by observation and photography under a light microscope.

### 2.9. Immunohistochemical analysis

At 24 weeks post-surgery, the sciatic nerve and target muscle of dogs were excised, routinely post-fixated, gradient-dehydrated with sucrose, and frozen-sectioned. After wash, the tissue sections were blocked using immunostaining blocking solution (Beyotime) at room temperature for 2 h. Nerve sections were reacted with anti-S100 (ab4066, Abcam, 1:400) and anti-NF200 (N4142, Sigma-Aldrich, 1:400). Muscle sections were reacted with anti-laminin (1:500, Abcam) overnight at 4 °C. The nerve or muscle sections were incubated with labeled secondary antibodies at 37 °C for 2 h. To evaluate the neuromuscular junctions (NMJs), 20 µm-thick longitudinal muscle sections were incubated with anti-NF200 and co-stained with α-bungarotoxin (α-BTX,1:200, Sigma-Aldrich). After being counterstained with Hoechst 33258, the sections were mounted and observed under confocal or fluorescent microscopy. The images were quantitatively analyzed by Image J software.

### 2.10. Harvesting of rat motor and cortical neurons

After pregnant SD rats at 14 days of gestation were sacrificed, the fetal rats were taken out from the abdominal cavity and placed in pre-cooled Leibovitz's L-15 medium (Gibco). To harvest motor neurons, the spinal cord of fetal rats was separated under a dissecting microscope, digested with 0.125 % trypsin at 37 °C for 30 min, and mechanically dissociated to obtain single-cell suspension. The rat motor neurons were purified in 15 % OptiPrep gradient centrifugation solution (Sigma-Aldrich). To harvest cortical neurons, the cerebral cortex of fetal rats was isolated under a dissecting microscope, and the tissue was cut and digested with 0.25 % trypsin at 37 °C for 15 min. Digestion was terminated by DMEM medium supplemented with 10 % FBS. The rat cortical neurons were mixed thoroughly and filtered with a 400-mesh sieve.

The acquired rat motor and cortical neurons were counted and seeded onto dishes with poly-L-lysine pre-coated coverslips and cultured in a 37 °C incubator with 5 % $CO_2$ for 4 h, and then the medium was replaced with neurobasal medium supplemented with 2 % B27, 1 % glutamax, and 1 % penicillin/streptomycin (all from Gibco).

### 2.11. Transfection of cells and EVs

The miRNAs mimics, inhibitors, or siRNA and their respective negative controls (5 nmol/tube) were constructed and synthesized by RiboBio (Guangzhou, China), diluted into 20 µM stock solution by adding 250 µl of diethylpyrocarbonate water and stored at −20 °C. For cell transfection, the stock solution of miRNA mimics or siRNA was diluted with Opti-MEM to the concentration of 200 nM, gently mixed with Lipofectamine RNAiMAX reagent (Thermo Fisher Scientific, Cleveland, OH, USA), and incubated at room temperature for 10 min. The rat motor or cortical neurons were treated with the medium containing transfection complex for 12 h, and then replaced with neuro-basal medium supplemented with 2 % B27, 1 % glutamax, and 1 % penicillin/streptomycin (all from Gibco).

For EV transfection, miR-30b-5p inhibitor was transfected into SKP-SC-EVs by using Exo-Fect™ Exosome Transfection Reagent (System Bio, USA) according to the manufacturer's instructions. Specifically, 120 µl sterile PBS containing $10^7$ EVs, 10 µl Exo-Fect solution, 20 µl miR-30b-5p inhibitors (20 pmol) were mixed in a clean 1.5 ml tube to forma 150

μl transfection system. After gently mixing, the components were incubated at 37 °C in a shaker for 10 min, then immediately place on ice. The 30 μl of ExoQuick-TC reagent was added to the system for thorough mixing. The system was placed on ice for 30 min and then centrifuged at 13000 rpm for 3 min. After the supernatant was discarded, the transfected EVs were resuspended in 300 μl of PBS. The 150 μl of transfected EVs were added to approximately $10^5$ cells per well in a 6-well culture plate grown in exosome-depleted FBS. The ratio can be scaled up or down depending upon experimental requirements.

### 2.12. Axon growth and regeneration in microfluidic devices

Microfluidic devices (150 μm microgroove barrier, cat. SND150, Xona Microfluidics, Timecula, CA, USA) were assembled as described previously [22]. They were washed, soaked and sterilized under ultraviolet irradiation and then they were attached to the poly-L-lysine pre-coated petri dishes to form 2 cell chambers connected by more than 100 channels (150-μm long). Rat neurons were resuspended, and 5 μl of neuron suspension ($1 \times 10^7$ cells/ml) was loaded into the soma chamber of the microfluidic device to be cultured at 37 °C for 4 h. Following cell adherence, rat motor neurons were replaced with neurobasal medium containing transfection complex to perform miRNA transfection, while rat cortical neurons were cultured for 7 d before transfection. For axon growth from rat neurons, the fresh medium was changed 12 h after transfection, and immunofluorescence staining was performed after further culture for 72 h. For axon regeneration, rat neurons were further cultured for 3 d after transfection, the pressure of vacuum pump was adjusted to above 0.2 Mpa, and the axon compartment was aspirated 3 times (30 s/time) to ensure complete axon transection. After adding culture medium for 24 h, rat neurons were labeled by primary anti-Tuj1 antibody (ab7751, Abcam, 1:500) and an FITC conjugated secondary antibody, followed by observation under an inverted fluorescence microscope (DMI8, Leica, Mannheim, Germany). The length of the top 50 longest axons (n = 3) was measured by Image J software. For experimental protocols, see Fig. S2.

### 2.13. High-throughput transcriptome sequencing and bioinformatic analysis

After transfection of neurons with miR-30b-5p mimic or negative control for 12 h, the medium was replaced with neurobasal medium for 48 h culture. Total RNA was isolated from neurons and purified using TRIzol reagent (Invitrogen, Carlsbad, CA, USA) according to the manufacturer's instructions. The RNA purity and concentration were quantified by NanoDrop ND-1000 (NanoDrop, Wilmington, DE, USA), and the RNA integrity was assessed by Bioanalyzer 2100 (Agilent, CA, USA) with RIN value > 7.0 and verified by denatured agar-gel electrophoresis. Poly (A) RNA was purified from 1 μg total RNA using Dynabeads Oligo (dT) 25–61005 (Thermo Fisher, CA, USA), and fragmented into small pieces using Magnesium RNA Fragmentation Module (NEB, cat.e6150, USA) at 94 °C for 5 min. Then, the first and second strands of cDNA were synthesized and the double-stranded cDNA ends were repaired and joined before real-time quantitative polymerase chain reaction (qPCR) amplification and purification were carried out. Sequencing was performed on lumina NovaseqTM 6000 (LC-Bio Technology CO., Ltd., Hangzhou, China) following the vendor's recommended protocol after library quality. The mRNA expression level was analyzed using StringTie software by calculating FPKM (FPKM = total exon fragments/[mapped reads (millions) × exon length (kb)]), and the differentially expressed genes were selected (fold change <0.667, $P < 0.05$) by R package edger before bioinformatic analyses to identify Gene Ontology (GO) function terms and Kyoto Encyclopedia of Genes and Genomes (KEGG) pathways by using the Database for Annotation, Visualization and Integrated Discovery (DAVID, https://david.ncifcrf.gov/).

In addition, some freely available online databases, such as miRWalk (http://mirwalk.uni-hd.de/), TargetScan (http://www.targetscan.org/)

and miRDB (http://www.mirdb.org/) databases were applied to search for the targets of miRNAs. The Venn diagram was used for graphical depiction of the intersections among multiple datasets or documents.

### 2.14. Dual luciferase reporter gene assay

The possible binding sites between miR-30b-5p and Sin3a 3′UTR were predicted by miRWalk database (http://mirwalk.uni-hd.de/). For luciferase reporter assay, Sin3a-3′UTR wild-type (WT) or mutant-type (Mut) plasmids (RiboBio) were constructed and co-transfected into HEK293T cells with miR-30b-5p mimic or miRNA-negative control (miR-NC). The combinations of transfected plasmids were as follows: Sin3a-WT + miR-NC, Sin3a-WT + miR-30b-5p mimic, Sin3a-Mut + miR-NC and Sin3a-Mut + miR-30b-5p mimic respectively. At 48 h after transfection, cells were lysed to measure the luciferase activity of the lysates using the Dual-Luciferase Reporter Assay System (Promega, Inc., Madison, WI, USA) according to the manufacturer's instructions. Firefly luciferase values were normalized to Renilla luciferase and the ratio of Firefly/Renilla values was reported as relative luciferase activity.

### 2.15. qPCR examination

Total RNA was extracted and purified by TRIzol method, and the purity and concentration of RNA were detected by NanoDrop ND-1000. The expression of miRNAs was quantified by qPCR using miDETECT A Track™ miRNA qRT-PCR Starter kit (RiboBio) on the Bio-Rad CFX system (Bio-Rad, Hercules, CA) under the following conditions: 95 °C denaturation for 10 min, and 40 cycles of amplification at 95 °C for 10 s, at 60 °C for 20 s and at 70 °C for 1 s qPCR results were analyzed using the comparative threshold cycle method ($2^{-\Delta Ct}$) and normalized to U6 small nuclear RNA (U6 snRNA).

cDNA was synthesized by the HiScript III 1st Strand cDNA Synthesis kit (Vazyme, Jiangsu, China). The primers were designed and synthesized by Sangon Biotech Co., Ltd. (Shanghai, China). According to the instructions of ChamQ Universal SYBR qPCR Master Mix kit (Vazyme, Najing, Jiangsu, China), forward primers, reverse primers and templates were added to the reaction system, and qPCR was performed on the Bio-Rad CFX system under the following conditions: 95 °C denaturation for 15 min, and 40 cycles of amplification at 94 °C for 15 s, at 55 °C for 30 s and at 70 °C for 30 s. The relative mRNA level was quantified using glyceraldehyde 3-phosphate dehydrogenase (GAPDH) as an internal control. Sequences of primers are presented in Table 1.

### 2.16. Western blot analysis

The cells were harvested and lysed by M-PERTM Mammalian Protein Extraction Reagent (Thermo Scientific, Rockford, IL, USA) containing protease and phosphatase inhibitors (Beyotime, Shanghai, China), and the protein concentration was determined using BCA Protein Assay kit (Beyotime). Protein samples were mixed with 5 × SDS-PAGE loading buffer (Beyotime) and boiled for 10 min. A total of 20 μg of protein was

**Table 1**
Primer sequences of miRNA and target genes.

| Name | Primer | Sequences |
|---|---|---|
| rno-miR-30b-5p | | UGUAAACAUCCUACACUCAGCU |
| Sin3a | Forward primer | AATCCCTCCATTGCTGTTCCCATTG |
| | Reverse primer | GCTCTCGCCAGACCTTGTTGAAG |
| Socs3 | Forward primer | GCCTCAAGACCTTCAGCTCCAAG |
| | Reverse primer | CGGTTACGGCACTCCAGTAGAATC |
| Kremen1 | Forward primer | CGCTGCCCACTCTTCCAAAGTC |
| | Reverse primer | TACACGGTCCATCCTTCCACTCTG |
| Rtn4r | Forward primer | TCCCGACAACACCTTCCGAGAC |
| | Reverse primer | GCACACGAGCCACATGGTTCTG |
| GAPDH | Forward primer | TCTCTGCTCCTCCCTGTTC |
| | Reverse primer | ACACCGACCTTCACCATCT |

separated using 10 % SDS-PAGE and then transferred onto poly-vinylidene fluoride membranes (Merck Millipore, Billerica, MA, USA). Subsequently, the membranes were blocked in Tris buffered saline/Tween 20 (TBST) solution containing 5 % skim milk for 2 h at room temperature and then incubated overnight at 4 °C with the following primary antibodies: anti-Sin3a (14638-1-AP, Proteintech, 1:1000), anti-GAP43 (ab75810, Abcam, 1:1000), anti-*p*-STAT3 (9145, CST, 1:1000), anti-STAT3 (30835S, CST, 1:1000), anti-*p*-CREB (9198, CST, 1:1000), anti-CREB (9197, CST, 1:1000), anti-*p*-ERK1/2 (4370T, CST, 1:1000), anti-ERK1/2 (4695T, CST, 1:1000), anti-*p*-AKT (9272S, CST, 1:1000), anti-AKT (9271S, CST, 1:1000), anti-*p*-S6 (5364T, CST, 1:1000), anti-S6 (2217S, CST, 1:1000), anti-GAPDH (60004-1-Ig, Proteintech, 1:5000) and anti-β-actin (AC004, Abclonal, 1:10000). GAPDH or β-actin was used as the internal control to normalize protein loading. After wash with TBST (10 min/time), the membranes were incubated with horse-radish peroxidase-conjugated AffiniPure goat anti-mouse IgG (ab205719, Abcam, 1:5000) or anti-rabbit IgG (ab205718, Abcam,1:5000) for 2 h at room temperature. After wash with TBST, protein bands were visualized with the Pierce ECL Western Blotting Substrate kit (Thermo Scientific) on Tanon 5200 Chemiluminescent Imaging System imaging system.

### 2.17. Statistical analysis

Statistical analysis was performed with GraphPad Prsim 8.0 software (Inc, San Diego, CA, USA). Data are presented as means ± SD/SEM. A 2-tailed Student's *t*-test was used to determine statistical differences between two groups, and one-way ANOVA plus post-hoc Dunnett's test for comparisons among multiple groups. *P* value < 0.05 was considered statistically significant.

## 3. Results

### 3.1. Identification of SKP-SCs and SKP-SC-EVs

SKPs were isolated and purified from the skin of newborn rats by an enzyme digestion method. Immunoanalysis indicated that SKPs expressed nestin (a marker for ectodermal neural stem cells), versican (a marker for hair follicle dermal papilla dermal sheaths), and Ki67 (a marker for proliferation marker), thus confirming their cell purity [15].

SKPs were induced to differentiate into SCs in a specific medium. The acquired SKP-SCs displayed the long-spindle morphology and side-by-side alignment, and showed positive expression of SC-specific markers including S100β, GFAP, and p75NTR under immunostaining conditions, while the average purity of SKP-SCs of 98.5 % (S100β positive percentage) suggested a high efficiency of SKPs differentiation into SKP-SCs [15]. In this study, SKP-SCs were cryopreserved at early passages for use, and SKP-SCs at passage 15 to 17 still kept the desired purity in terms of their co-expression of S100 and GFAP (Fig. S3A).

TEM examination revealed that the isolated SKP-SC-EVs were round vesicles of uniform size with a membrane structure of approximately 50–200 nm in diameter (Fig. S3B). Nanoparticle tracking analysis showed that the particle size distribution of SKP-SC-EVs ranged from 30 to 300 nm (Fig. S3C). Moreover, Western blot analysis indicated that SKP-SC-EVs were immunopositive for CD9, CD63 and Hsp70 compared to SKP-SCs (Fig. S3D).

### 3.2. Motor function recovery

After surgery, no obvious systemic symptoms or local inflammation were observed in all dogs. Their locomotor function gradually recovered. Dogs began to stand with their palms touching the ground at 4 weeks post-surgery, and were able to walk easily at 12 weeks post-surgery.

The motor coordination of 2 hind legs during walking and the posture of standing on hind legs were compared among 3 groups. At 12

weeks post-surgery, the injured limbs of dogs in both autograft and TENG groups manifested different degrees of claudication, lack of coordination of 2 hind legs, incapability of load-bearing, and abnormality of metatarsophalangeal joint plantar flexion, whereas dogs in the EV-TENG group showed significant improvement (Fig. 1A–C). At 24 weeks post-surgery, dogs in the EV-TENG group could stand upright on 2 hind legs, which coordinated well with each other in terms of movements. Simultaneously, locomotor functional recovery of the injured limb in autograft group approached that in the EV-TENG group, and was better than that in the TENG group (Fig. 1B–D). At 12 and 24 weeks post-surgery, the hind limb function scores in the autograft groups were significantly higher than those in the TENG group. At 24 weeks post-surgery, the hind limb function score in the EV-TENG group was significantly higher than that in the TENG group. Moreover, the hind limb function scores in the EV-TENG group and the autograft group were similar, with no statistically significant difference (Fig. 1E). Collectively, chitosan/PLGA-based, SKP-SC-EVs-containing TENGs (EV-TENGs) significantly accelerated the restoration of motor function in dogs.

### 3.3. Recovery of electrical conduction and nerve pathway integrity

At 24 weeks post-surgery, electrophysiological tests were performed on the dogs in the 3 groups (Fig. 2A). The CMAP amplitude and MNCV measured on the injured side in the EV-TENG group were similar to those in the autograft group (*P* > 0.05), but significantly greater than those in the TENG group (*P* < 0.05) (Fig. 2B and C). Certainly, the values of both parameters measured on the contralateral, uninjured side were significantly higher than those measured on the injured side for each animal.

FG retrograde tracing showed that at 24 weeks post-surgery, the percentage of FG-labeled sensory neurons and the total number of FG-labeled motor neurons in EV-TENG group were similar to that in autograft group (*P* > 0.05), but significantly greater than that in TENG group (*P* < 0.05) (Fig. 2D–G), suggesting that EV-TENGs encouraged the recovery of nerve electrical conduction and nerve pathway integrity in dogs.

### 3.4. Regeneration of the injured sciatic nerve

At 24 weeks post-surgery, the chitosan/PLGA-based NGC body in the TENG or EV-TENG group was degraded, absorbed and replaced by nerve-like tissues, which had been connected to the proximal and distal nerve stumps, while the re-implanted nerve tissue in the autograft group was integrated to the intact nerve through both junctions without obvious demarcation at 2 nerve stumps (Fig. 3A). The regenerated nerve tissue was thicker and the blood vessels were more abundant in the EV-TENG group than they were in the TENG group. Immunostaining was performed to compare the status of sciatic nerve regeneration among 3 groups (Fig. 3B). Moreover, the fluorescence intensity of NF200-positive nerve fibers in the middle segment of the regenerated nerve was significantly higher in the EV-TENG group than that in TENG group, and was similar to that in autograft group (Fig. 3C). TEM demonstrated the ultrastructure of regenerated nerve fibers (Fig. 3D), while the lamellae structure of regenerated myelin sheaths provided further evidence. The myelinated axon diameter, myelin sheath thickness, and myelin lamellar number at the distal end of the regenerated nerve in the EV-TENG group were significantly greater than those in the TENG group, but were close to those in the autograft group (Fig. 3E–G). These findings indicated that EV-TENGs facilitated the process of axon growth and myelination in dogs.

### 3.5. Target muscle reinnervation and NMJ reconstruction

At 24 weeks post-surgery, the TA and GC muscles on the bilateral sides were dissected for observation. The GC muscles on the injured side in TENG and EV-TENG groups displayed prominent atrophic fibrosis
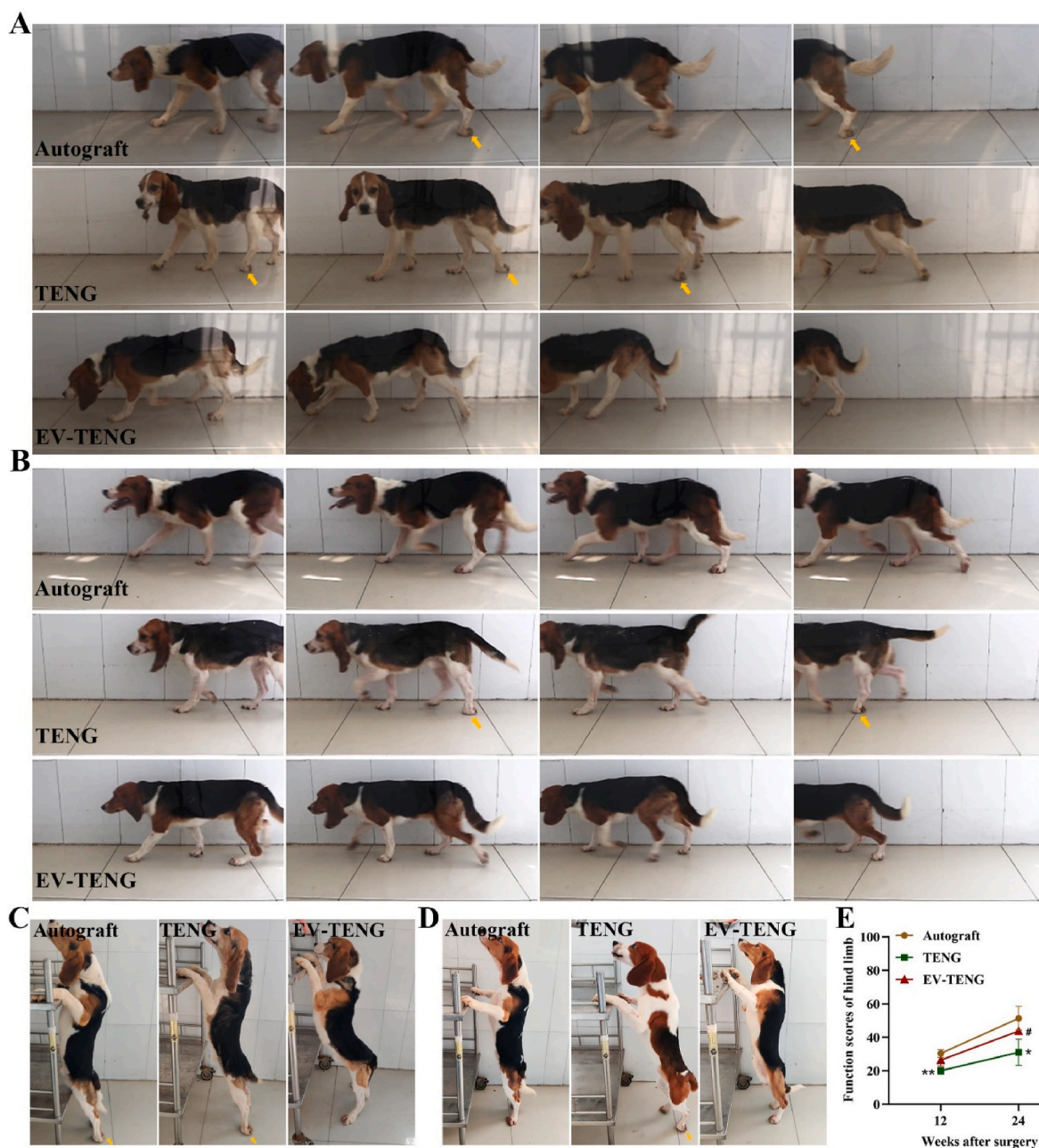
**Fig. 1.** Evaluation of motor function in dogs post-surgery. Sequential video frames showing coordination in the motion of 2 hind limbs when dogs were walking at 12 (**A**) and 24 (**B**) weeks post-surgery respectively. Photographs demonstrating the posture of standing on hind limbs of dogs at 12 (**C**) and 24 (**D**) weeks post-surgery respectively. The yellow arrows indicate poor functional recovery featured by incapability of load-bearing, a lack of coordination between the injured and contralateral, uninjured limbs, or abnormality of the metatarsophalangeal joint plantar flexion. (E) Histogram comparing the function score of hind limb among 3 groups. All data are presented as mean ± SD. *$P < 0.05$ and **$P < 0.01$ vs the autograft group; #$P < 0.05$ vs the TENG group.

with loss of normal appearance and texture, while the GC muscles on the injured side in the autograft group were similar to those on the contralateral, uninjured side, exhibiting a lustrous red color and relatively soft texture (Fig. 4A). The wet weight ratio (injured side/contralateral side) of TA or GC muscles was significantly higher in the EV-TENG group than in the TENG group, but was slightly lower in the EV-TENG group than in the autograft group without significant difference (Fig. 4B). The average cross-sectional area for either of 2 target muscles was significantly larger in the EV-TENG group than in the TENG group (Fig. 4C). Morphological features of muscle fibers were evaluated using immunostaining and Masson trichrome staining. Laminin immunostaining revealed that the muscle cells were larger and more closely arranged in the EV-TENG group than in the TENG group (Fig. 4D).

Masson trichrome staining showed severe muscle atrophy appearing in the TENG group, featured by the existence of large amounts of collagen fibers, whereas the larger muscle cells and the fewer collagen fibers were noted in EV-TENG and autograft groups than in the TENG group (Fig. 4E).

In terms of TEM images, myofilaments and sarcomeres were neatly arranged, the Z-lines were clear, and a large number of mitochondria with intact structure were uniformly distributed in the myofibrils for GC muscles on the contralateral, uninjured side. In contrast, the filament arrangement was slightly irregular, and the morphology of mitochondria was slightly abnormal for GC muscles on the injured side in the autograft group at 24 weeks post-surgery. Importantly, the structure of GC muscles on the injured side in EV-TENG group was much more intact
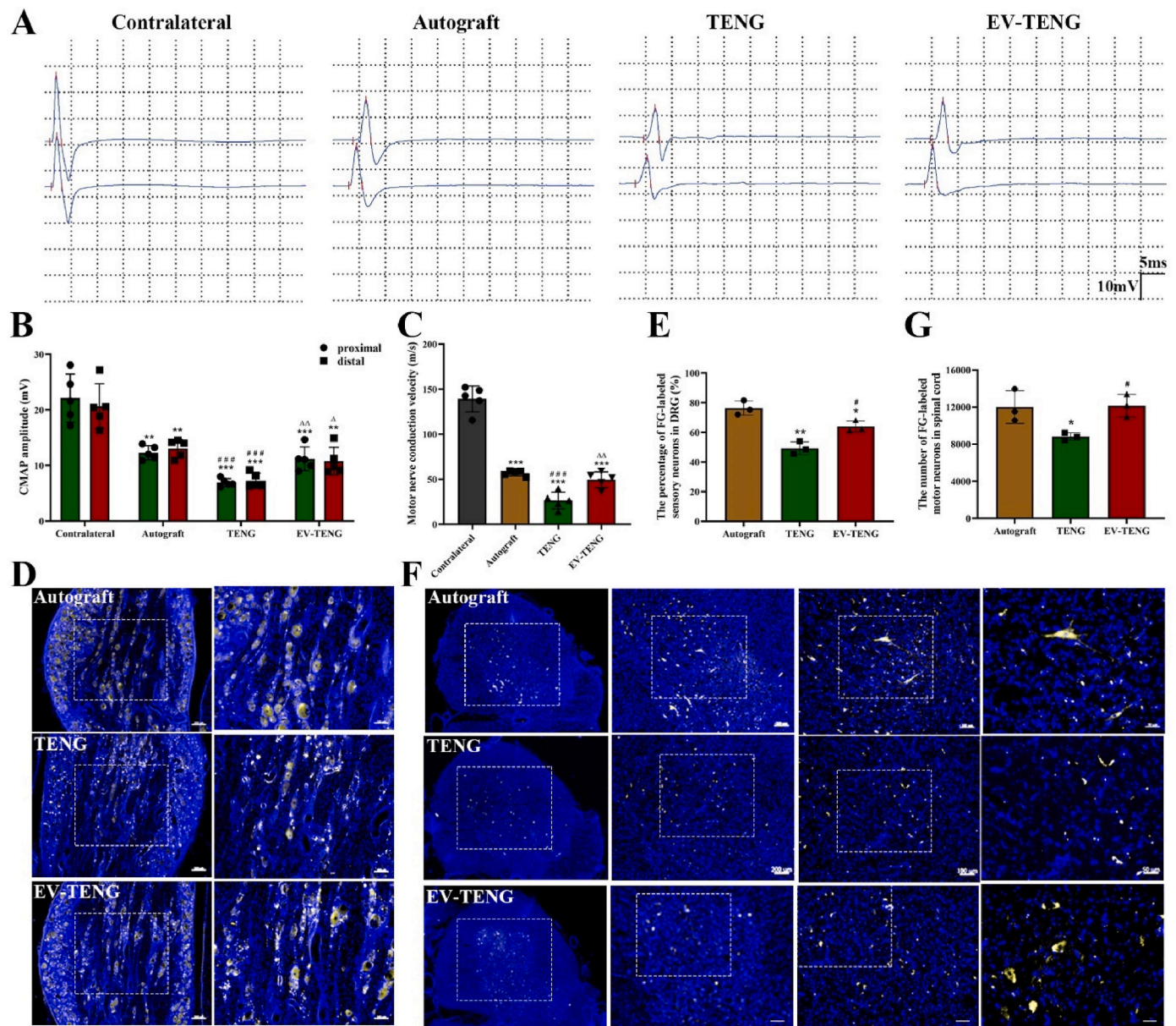
**Fig. 2.** Electrophysiological evaluation and FG retrograde nerve tracing. (A) Representative CMAP images recorded on the injured or contralateral side in the 3 groups (n = 5 each) at 24 weeks post-surgery with a stimulation intensity of 10 mA. (**B**) Histogram comparing distal and proximal CMAP amplitudes among different groups (n = 5 per group). (**C**) Histogram comparing MNCV values among different groups (n = 5 per group). All data are presented as mean ± SD. $**P < 0.01$ and $***P < 0.001$ vs the contralateral side; $###P < 0.001$ vs the autograft group; $\triangle\triangle P < 0.01$ and $\triangle\triangle\triangle P < 0.001$ vs the TENG group. (**D**) Representative image of FG (golden)-labeled sensory neurons in DRGs on the injured side of 3 groups with Hoechst (blue) nucleus labeling. Scale bars = 200 μm (left) and 100 μm (right). (**E**) Histogram comparing the percentage of FG-labeled sensory neurons in DRGs among 3 groups (n = 3 per group). (**F**) Representative image of FG (golden)-labeled motor neurons in the spinal cord. Scale bars = 500 μm, 200 μm, 100 μm and 50 μm (from left to right). (**G**) Histogram showing the total number of FG-labeled motor neurons in spinal cord among 3 groups (n = 3 per group). All data are presented as mean ± SD. $*P < 0.05$ and $**P < 0.01$ vs autograft group; $#P < 0.05$ vs TENG group.

than that in TENG group, and close to that in autograft group at 24 weeks post-surgery. (Fig. 4F). NF200 and α-BTX double staining indicated that the NMJ structure in EV-TENG group was larger and more complete than that in TENG group, similar to that in autograft group (Fig. 4G). The above observations suggested that chitosan/PLGA-based, SKP-SC-EVs-containing TENGs (EV-TENGs) significantly stimulated the target muscle reinnervation and NMJ reconstruction in dogs.

### 3.6. Screening of miRNAs in SKP-SC-EVs

To gain insight into the molecular mechanism responsible for the promotive effect of SKP-SC-EVs on sciatic nerve regeneration, we investigated the molecular composition of SKP-SC-EVs. By miRNA sequencing, 279 known miRNA matures were found in SKP-SC-EVs, and the top 60 highly expressed miRNAs were ranked according to their abundance (Table 2). Through literature review and functional annotation analysis, 16 miRNAs (miR-30b-5p, miR-23a-3p, miR-103-3p, miR-26a-5p, miR-99a-5p, miR-25-3p, miR-29a-3p, miR-27a-5p, miR-204-5p, miR-222-3p, miR-92a-3p, miR-20b-5p, miR-34a-5p, miR-17-5p, miR-22-3p and miR-93-5p) were selected for further investigation based on their possible relationship with nerve regeneration.

Microfluidic devices were used to assess the impact of the above 16 miRNAs on axon growth of rat motor neurons. After neurons were transfected individually with each of the 16 miRNAs, transfection with
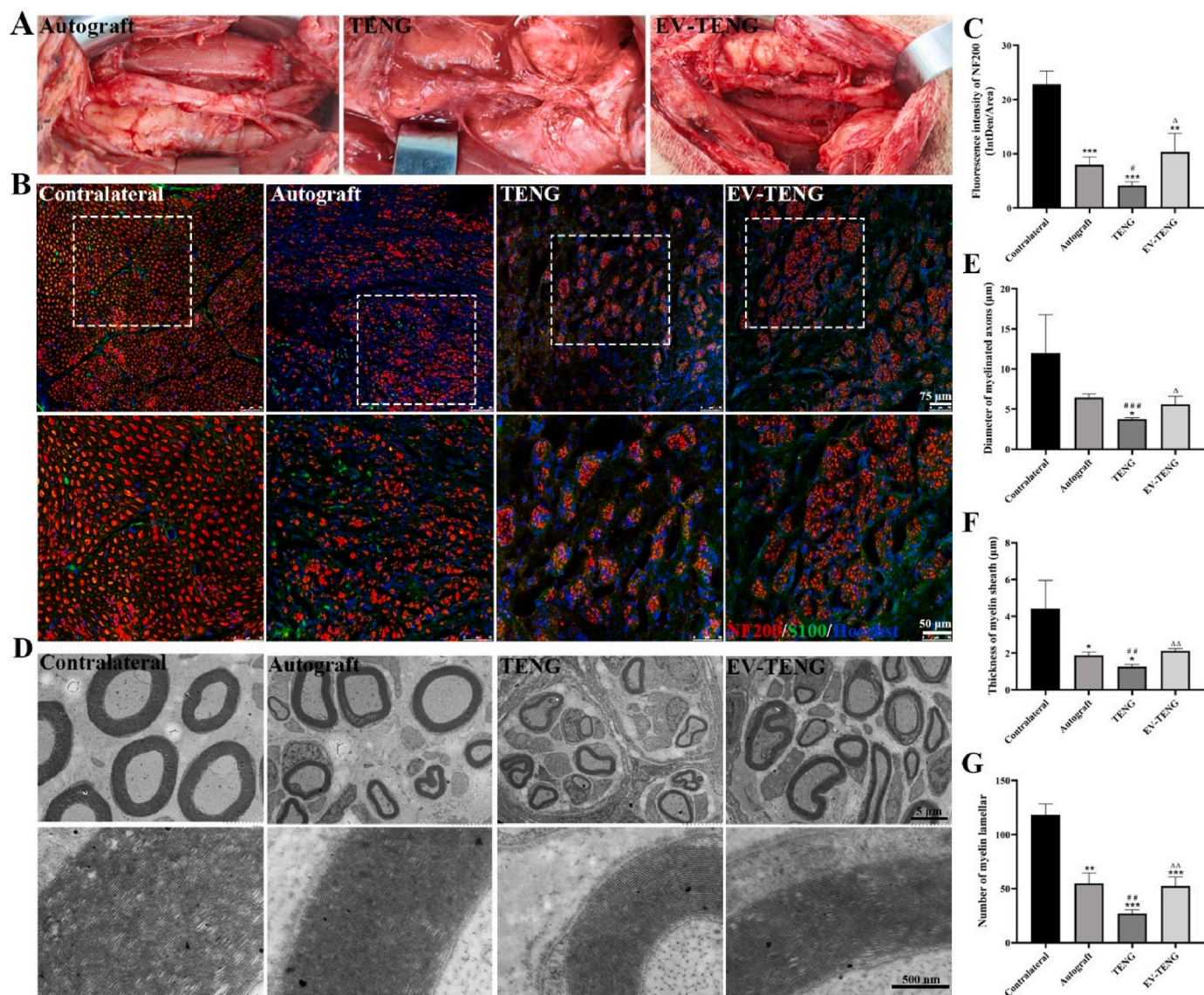
**Fig. 3.** Morphological analysis of regenerated nerves. (A) Gross view of the regenerated sciatic nerve in the 3 groups at 24 weeks post-surgery. (B) Immunostaining images of cross-sections of the middle portion of dog sciatic nerve on the injured side or the contralateral, uninjured side in the 3 groups at 24 weeks post-surgery. Axons and myelin sheaths were immunostained with NF200 (red) and S100 (green) respectively, and nucleus were counterstained with Hoechst (blue). Scale bars = 75 (upper) and 25 μm (lower). (C) Histograms showing statistical analysis for the fluorescence intensity of NF200-positive nerve fibers. (D) TEM images showing the morphology of regenerated nerve fibers in the 3 groups at 24 weeks post-surgery. Scale bars = 5 (upper) and 500 nm (lower). Histograms comparing the diameter of myelinated axons (E), the thickness of myelin sheath (F), and the number of myelin lamellar (G) (n = 3, 6 random fields per dog). Data are presented as mean ± SD. $*P < 0.05$, $**P < 0.01$ and $***P < 0.001$ vs the contralateral nerve; $^{##}P < 0.01$ and $^{###}P < 0.001$ vs the autograft group; $^{\triangle}P < 0.05$ and $^{\triangle\triangle}P < 0.01$ vs TENG group.

13 out of 16 miRNAs (except miR-17-5p, miR-22-3p and miR-93-5p) supported axon regeneration of rat motor neurons to varying degrees compared to cells transfected with blank control or with miR-NC (Fig. 5A).

Axon regeneration of miRNA-transfected rat motor neurons was quantitatively examined. Statistical analysis indicated that the average length of regenerated axons in miR-30b-5p, miR-23a-3p, or miR-103-3p overexpression groups was significantly greater than that in the miR-NC group, suggesting that these 3 miRNAs effectively promoted axon regeneration of rat motor neurons (Fig. 5B).

Similarly, microfluidic devices were also applied to assess the impact of the above 16 miRNAs on axon growth of rat cortical neurons. After the 16 miRNAs were individually transfected into neurons, transfection with 14 out of the 16 miRNAs (excluding miR-26a-5p and miR-92a-3p) supported axon regeneration of rat cortical neurons to varying degrees as compared to transfection with the blank control or miR-NC (Fig. 6A).

To quantitatively evaluate axon regeneration of miRNA-transfected rat cortical neurons, statistical analysis indicated that the average length of regenerated axons in miR-30b-5p, miR-29a-3p, miR-103-3p, miR-17-5p, miR-27a-5p, miR-22-3p and miR-23a-3p overexpression groups was significantly greater than that in the miR-NC group, suggesting that these 7 miRNAs effectively promoted axon regeneration of rat cortical neurons (Fig. 6B). Moreover, chondroitin sulfate proteoglycan 4 (CSPG4) was used to treat rat cortical neurons before miRNA transfection because CSPG4 is known to serve as a major extracellular matrix for inhibiting axon regeneration in glial scars following central nervous system injury [23]. After rat cortical neurons were seeded in poly-L-lysine-coated culture dishes pre-added with 30 ng/ml CSPG4, the cells were transfected with miR-29a-3p, miR-30b-5p, miR-103-3p or miR-17-5p mimic. Immunostaining revealed that these 4 miRNAs enhanced axon regeneration of rat cortical neurons after CSPG4 treatment compared to blank control (Fig. 6C). Statistical analysis showed
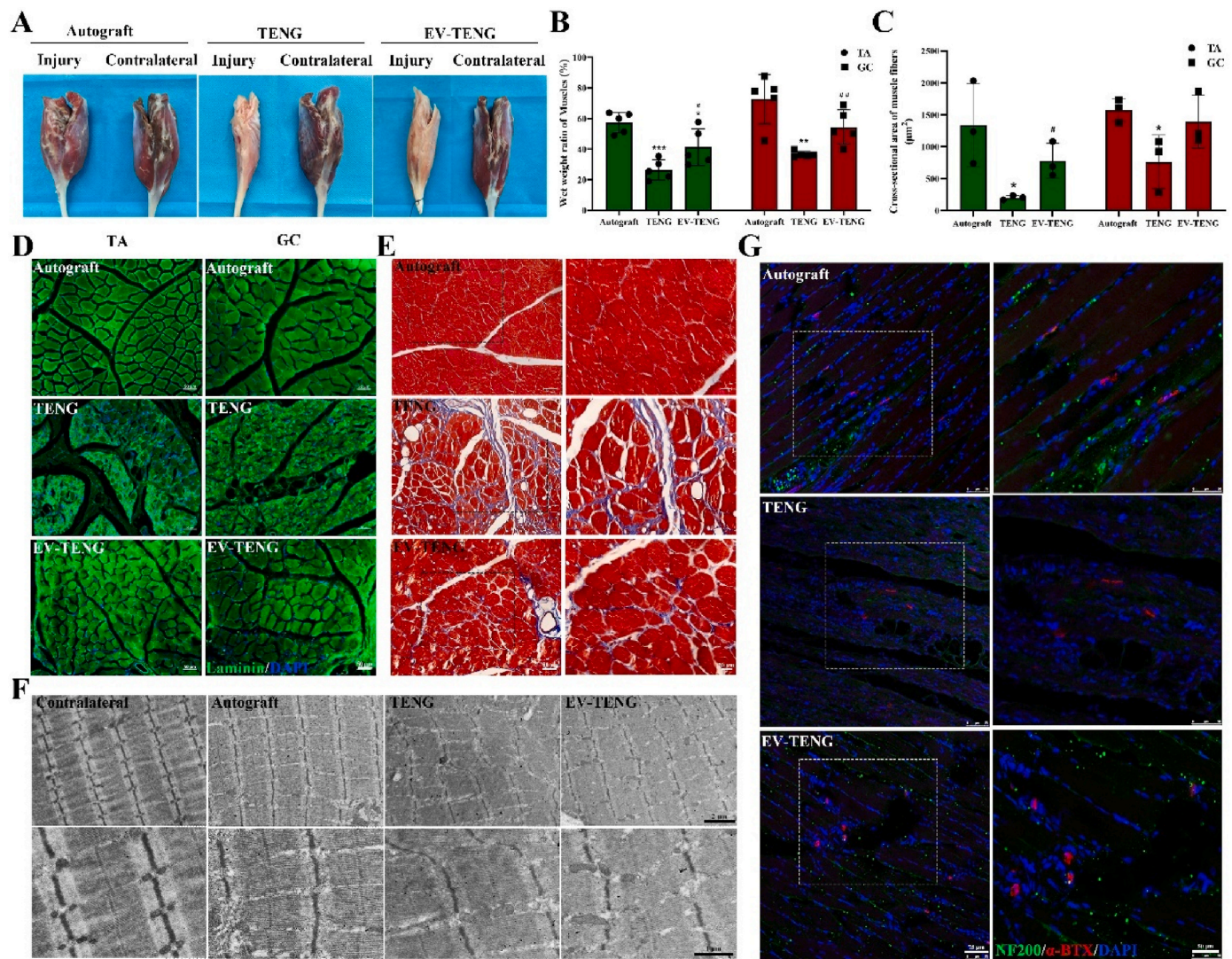
**Fig. 4.** Histological examination and morphometric analysis of target muscles and NMJs. (A) Gross view of GC muscles on the injured and contralateral, uninjured sides in 3 groups at 24 weeks post-surgery. (**B**) Histogram comparing the wet weight ratio (injured side/contralateral side) of GC or TA muscles among the 3 groups (n = 5) at 24 weeks post-surgery. (**C**) Histogram comparing the cross-sectional area of target muscle fibers (n = 3, 6 random fields per dog) at 24 weeks post-surgery. (**D**) Immunostaining images of the cross-section of GC muscles in 3 groups at 24 weeks post-surgery, showing muscle cells with laminin staining (green), and DAPI nucleus counterstaining (blue). Scale bar = 50 μm. (**E**) Masson trichrome staining images of the cross-sections of GC muscles in 3 groups at 24 weeks post-surgery, showing muscle cells (red) and collagen (blue). Scale bar = 50 μm (left) and 20 μm (right). (**F**) Morphology of GC muscles in 3 groups at 24 weeks post-surgery, as observed via TEM. Scale bar = 2 μm (upper) and 1 μm (lower). (**G**) Representative images of NMJs of longitudinal sections of GC muscles in 3 groups at 24 weeks post-surgery, where the nerve showed the NF200 expression (green), α-BTX expression (red) and Hoechst expression (blue). Scale bar = 75 μm (left) and 50 μm (right). All data are presented as mean ± SD. *$P < 0.05$, **$P < 0.01$ and ***$P < 0.001$ vs the autograft group; #$P < 0.05$ and ##$P < 0.01$ vs the TENG group.

that the average length of regenerated axons in miR-29a-3p, miR-30b-5p or miR-17-5p overexpression group was significantly greater than that in blank control or miR-NC group, suggesting that these 3 miRNAs effectively antagonized the inhibitory effect of CSPG4 on reinforcing axon regeneration of rat cortical neurons (Fig. 6D).

Moreover, 11 miRNAs, including miR-30b-5p, miR-103-3p, miR-23a-3p, miR-34a-5p, miR-99a-5p, miR-29a-3p, miR-25-3p, miR-27a-5p, miR-204-5p, miR-222-3p and miR-20b-5p, were noted to enhance axon regeneration of both rat motor and cortical neurons. Among these miRNAs, miR-30b-5p displayed the most prominent effect, suggesting that miR-30b-5p might be the key molecule responsible for the favorable effect of SKP-SC-EVs on axon regeneration *in vitro* (Fig. 6E).

### 3.7. SKP-SC-EVs promotion of axon growth and regeneration through miR-30b-5p targeting Sin3a

After treatment of motor neurons with SKP-SC-EVs, the expression level of miR-30b-5p in the cells significantly increased, implying that SKP-SC-EVs could deliver miR-30b-5p to motor neurons (Fig. 7A). In consequence, miR-30b-5p mimic was designed and synthesized *in vitro* for transfection of motor neurons to increase miR-30b-5p expression (Fig. 7B). Subsequently, the effect of miR-30b-5p on axon growth of motor neurons was investigated in a microfluidic device (Fig. 7Ca). Statistical analysis showed that the average length of axon growth in motor neurons transfected with miR-30b-5p mimics was significantly longer than that transfected with miR-NC (Fig. 7Cb). To study whether SKP-SC-EVs affect neuronal growth through their contained miR-30b-5p, miR-30b-5p inhibitor and its negative control were directly transfected into EVs. As shown in Fig. 7D, the expression level of miR-30b-5p

**Table 2**

The top 60 highly expressed miRNAs in SKP-SC-EVs.

| Number | miRNA name | Mean TMP | Number | miRNA name | Mean TMP |
|---|---|---|---|---|---|
| 1 | rno-miR-30a-5p | 148583.3465 | 31 | rno-miR-3570 | 4171.0422 |
| 2 | rno-let-7i-5p | 144712.1810 | 32 | rno-miR-181a-5p | 4170.0178 |
| 3 | rno-miR-21-5p | 106096.0795 | 33 | rno-miR-10a-5p | 4031.0330 |
| 4 | rno-miR-363-3p | 66951.9924 | 34 | rno-miR-93-5p | 3899.8583 |
| 5 | rno-miR-27b-3p | 62762.9038 | 35 | rno-miR-103-2-3p | 3665.6209 |
| 6 | rno-miR-146b-5p | 39624.0492 | 36 | rno-miR-221-3p | 3651.9016 |
| 7 | rno-miR-30e-5p | 29103.2300 | 37 | rno-miR-103-1-3p | 3642.7010 |
| 8 | rno-miR-24-2-3p | 24817.3843 | 38 | rno-miR-17-5p | 3412.7042 |
| 9 | rno-let-7f-5p | 24620.3088 | 39 | rno-let-7d-5p | 3274.1313 |
| 10 | rno-miR-26a-5p | 22136.2117 | 40 | rno-miR-181d-5p | 3137.1536 |
| 11 | rno-miR-22-3p | 21175.2037 | 41 | rno-miR-199a-3p | 3122.9647 |
| 12 | rno-miR-99a-5p | 20239.1859 | 42 | rno-miR-34a-5p | 3068.1239 |
| 13 | rno-miR-27a-5p | 18491.8301 | 43 | rno-miR-25-3p | 3061.0935 |
| 14 | rno-let-7g-5p | 17456.5721 | 44 | rno-miR-186-5p | 2978.3655 |
| 15 | rno-let-7c-5p | 15227.0951 | 45 | rno-miR-181b-5p | 2975.6603 |
| 16 | rno-miR-140-3p | 10363.5374 | 46 | rno-miR-98-5p | 2855.3230 |
| 17 | rno-miR-3074 | 9441.5256 | 47 | rno-miR-26b-5p | 2841.7468 |
| 18 | rno-miR-30c-5p | 9419.3456 | 48 | rno-miR-872-5p | 2767.1717 |
| 19 | rno-miR-34c-5p | 9075.8048 | 49 | rno-miR-125a-5p | 2735.1830 |
| 20 | rno-miR-9a-5p | 9015.8383 | 50 | rno-miR-92a-1-3p | 2668.0305 |
| 21 | rno-miR-7a-5p | 7918.6183 | 51 | rno-miR-34b-5p | 2534.9234 |
| 22 | rno-miR-23b-3p | 6615.0197 | 52 | rno-miR-30b-5p | 2481.8066 |
| 23 | rno-miR-23a-3p | 6282.8574 | 53 | rno-miR-222-3p | 2333.7123 |
| 24 | rno-miR-16-5p | 6242.4334 | 54 | rno-miR-20b-5p | 2253.7884 |
| 25 | rno-let-7b-5p | 6145.4766 | 55 | rno-miR-125b-5p | 2242.5797 |
| 26 | rno-miR-29a-3p | 6133.3230 | 56 | rno-miR-92a-3p | 2215.9037 |
| 27 | rno-miR-455-5p | 5667.0571 | 57 | rno-miR-92a-2-3p | 2215.9037 |
| 28 | rno-let-7a-5p | 5475.8888 | 58 | rno-miR-191a-5p | 2212.4293 |
| 29 | rno-miR-204-5p | 4464.1407 | 59 | rno-miR-148a-3p | 2097.4549 |
| 30 | rno-miR-100-5p | 4276.9805 | 60 | rno-miR-340-5p | 2042.5799 |

in the SKP-SC-EVs transfected with the miR-30b-5p inhibitor (miR-30b-5p inh-EVs) was significantly lower than that in the negative control transfected group (miR-NC-EVs). The microfluidic assay results showed that the average length of regenerated axons in the SKP-SC-EVs group was significantly higher than that in the blank control group. Moreover, the axon regeneration length in both the SKP-SC-EVs and miR-NC-EVs groups was significantly longer than that in the miR-30b-5p inh-EVs group, suggesting that SKP-SC-EVs promoted axon growth and regeneration of motor neurons through their contained miR-30b-5p (Fig. 7E).

To elucidate the molecular mechanism underlying the promotion of

axon regeneration in motor neurons by miR-30b-5p, high-throughput transcriptome sequencing was conducted on motor neurons transfected with miR-30b-5p mimics, and the expression changes of the top 100 differentially expressed genes were determined (Fig. 8Aa). Meanwhile, 2889 target genes of miR-30b-5p, as predicted by the common bioinformatics tools including miRWalk, TargetScan and miRDB databases, were intersected with 4294 significantly down-regulated genes, as determined by transcriptome sequencing, to identify 534 genes, including Kremen1, Sin3a, Rtn4r and Socs3 (Fig. 8Ab). KEGG enrichment analysis suggested that the target genes of miR-30b-5p were mainly involved in vasopressin-regulated water reabsorption, bile secretion and JAK-STAT signaling pathways (Fig. 8Ac). According to qPCR analysis, the mRNA expression level of Sin3a or Socs3 in motor neurons after transfection with miR-30b-5p mimics was significantly decreased compared to that after transfection with miR-NC. In contrast, the mRNA expression level of Kremen1 or Rtn4r in motor neurons after transfection with miR-30b-5p mimics was not significantly different from that after transfection with miR-NC, thus enlightening us to assume that Sin3a and Socs3 might be the target genes of miR-30b-5p (Fig. 8B).

To confirm this assumption, Western blot analysis was carried out to trace the change in Sin3a protein levels of motor neurons after transfection with miR-30b-5p mimic, and the result showed that miR-30b-5p overexpression significantly decreased the Sin3a protein level of motor neurons (Fig. 8C). Sin3a 3′UTR-WT or Sin3a 3′UTR-Mut were co-transfected with miR-30b-5p mimic into HEK293T cells to verify the target binding relationship between Sin3a and miR-30b-5p (Fig. 8Da). Interestingly, co-transfection of Sin3a WT with miR-30b-5p mimics significantly decreased the luciferase activity of HEK293T cells as compared to co-transfection of Sin3a WT with miR-NC, while co-transfection of Sin3a Mut with either miR-30b-5p mimics or miR-NC didn't significantly affect the similar luciferase activity of HEK293T cells, suggesting that Sin3a was the target gene of miR-30b-5p (Fig. 8Db).

Sin3a, as a transcription repressor, inhibits gene transcription by interacting with p53, STAT3 and other proteins. The mRNA level of Sin3a in motor neurons was significantly decreased by more than 50 % after interference (Fig. 8E). Assays in a microfluidic device demonstrated that the average length of regenerated axon in motor neurons transfected with Sin3a interference was significantly greater than that transfected with si-NC (Fig. 8F), and the promoting effect of Sin3a interference on axon regeneration of motor neurons was similar to that of Pten interference (Fig. 8G). These observations indicated that Sin3a might be a potential inhibitor of axon regeneration in motor neurons.

### 3.8. The miR-30b-5p-Sin3a/HDAC complex activated phosphorylation of ERK, STAT3 and CREB

The Sin3a/histone deacetylase (HDAC) complex, consisting of 8 core components, i.e., Sin3a, HDAC1, HDAC2, SAP18, SAP30, SDS3, RbAp46 and RbAp48 (Fig. 9Aa), affects the acetylation level of the proteins depending on HDAC1/2. Venn diagram displayed the intersection between 425 miRNAs identified by miRWalk databases, which target the Sin3a/HDAC complex, with 11 miRNAs in SKP-SC-EVs, which possess axon regeneration-promoting effects. This intersection yields 6 miRNAs, namely miR-30b-5p, miR-23a-3p, miR-34a-5p, miR-20b-5p, miR-25-3p and miR-27a-5p (Fig. 9Ab), which target different subunits of Sin3a/HDAC complex (Fig. 9Ac).

Subsequently, the effects of HDAC1 or HDAC2 interference on axon regeneration of motor neurons were investigated by a microfluidic device (Fig. 9Ba). Statistical analysis showed that the average length of regenerated axon of HDAC1 or HDAC2-interfered motor neurons was significantly greater than that of blank or negative control-interfered cells (Fig. 9Bb).

The expression levels of signaling pathway molecules related to nerve regeneration, including GAP43, *p*-STAT3/STAT3, *p*-CREB/CREB, *p*-ERK/ERK, *p*-AKT and *p*-S6, were detected by Western blot analysis
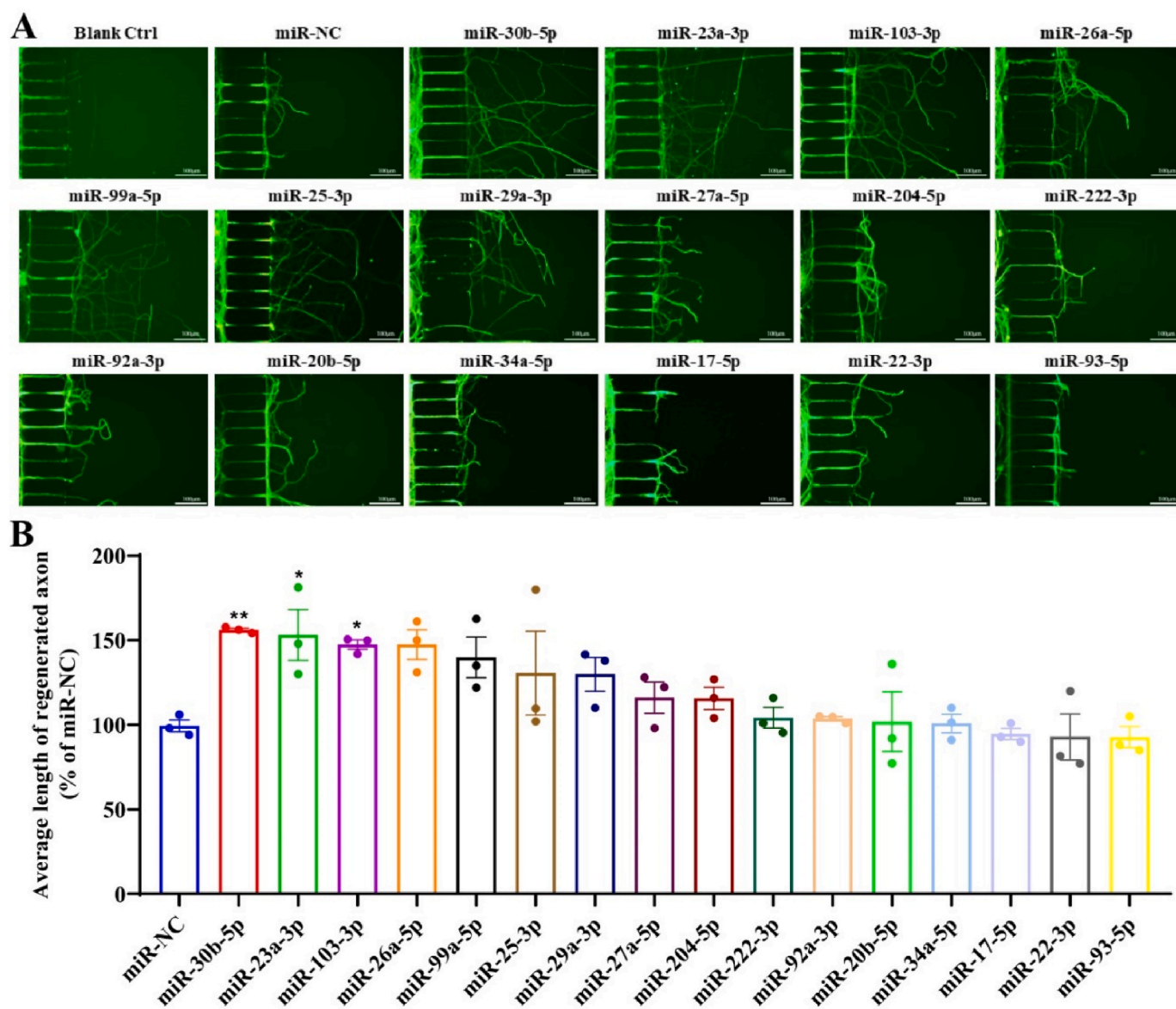
**Fig. 5.** Screening of miRNAs promoting axon regeneration of rat motor neurons in SKP-SC-EVs. (**A**) Immunostaining images of axon regeneration of motor neurons after miRNA transfection in microfluidic devices. The Blank Ctrl refers to non-transfected SCs, the miR-NC represents scramble-transfected SCs, and the rest indicates the corresponding miRNA mimic-transfected SCs. Scale bar = 100 μm. (**B**) Histogram comparing the average length of regenerated axons after miRNA transfection of motor neurons. Data are presented as a percentage relative to the miR-NC group (mean ± SEM). *$P < 0.05$ and **$P < 0.01$ vs miR-NC.

after miR-30b-5p overexpression. Transfection with miR-30b-5p mimics significantly increased the protein expression level of GAP43, *p*-STAT3/STAT3, *p*-CREB/CREB or *p*-ERK/ERK, suggesting that miR-30b-5p might promote axon regeneration of motor neurons by enhancing the phosphorylation of STAT3, CREB or ERK (Fig. 9C).

Moreover, the effect of miR-30b-5p agomir transfection on nerve regeneration was examined by immunofluorescence staining on the regenerating nerves harvested from rats with sciatic nerve crush injury on the 6th day post-injury. The fluorescence intensity of β-tubulin III (Tuj1) staining was significantly higher in miR-30b-5p agomir group than in miR-NC group (Fig. 9D), and the fluorescence intensity of NF200 or S100 staining was significantly higher in miR-30b-5p agomir group than in miR-NC group (Fig. 9E). The *in vivo* results suggested that miR-30b-5p overexpression could significantly improve sciatic nerve regeneration of rats after crush injury.

## 4. Discussion

In recent years, a great deal of effort has been invested in developing a promising design for TENGs to assist PNI repair. Our previous report has delineated that incorporation of SKP-SC-EVs represents a promising paradigm of TENG design [17]. In this study, we improved the application of SKP-SC-EVs in TENG fabrication by including SKP-SC-EVs into a chitosan/PLGA-based NGC, and we further evaluated the benefits of this new configuration of TENGs for sciatic nerve repair in dogs rather than rats.

NGCs, serving as the basic skeleton of TENGs, are capable of guiding and protecting axon regrowth from the injured nerve and maintaining sustainable delivery of biochemical cues [24]. The non-degradable, biologically inert silicone has been replaced by various classes of biodegradable, bioactive polymers as NGC materials. Chitosan, obtained from natural chitin by N-deacetylation, exhibits wide applications in tissue engineering, drug delivery, controlled release, and other biomedical fields because of its excellent biodegradability,
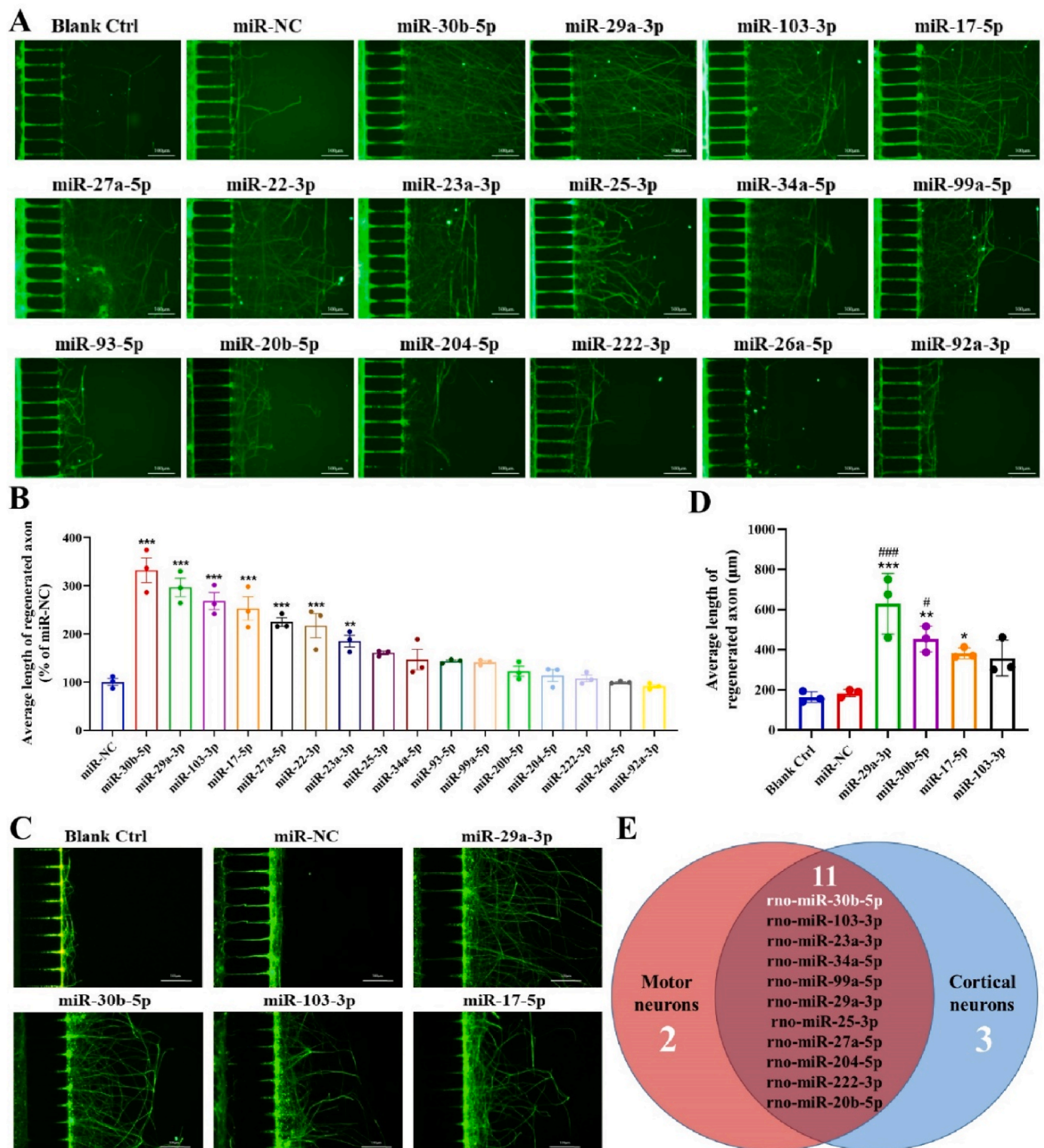
**Fig. 6.** Screening of miRNAs promoting axon regeneration of rat cortical neurons in SKP-SC-EVs. (A) Immunostaining images of axon regeneration in cortical neurons after miRNA transfection in microfluidic devices. Scale bar = 100 μm. (B) Histogram comparing the average length of regenerated axon after miRNA transfection. Data are presented as a percentage relative to miR-NC (mean ± SEM). **$P < 0.01$ and ***$P < 0.001$ vs miR-NC. (C) Immunostaining images of axon regeneration in cortical neurons after CSPG4 treatment in microfluidic devices. Scale bar = 100 μm. (D) Histogram comparing the average length of regenerated axons in miRNA-transfected cortical neurons after CSPG4 treatment. All data are presented as mean ± SEM. *$P < 0.05$, **$P < 0.01$ and ***$P < 0.001$ vs Blank Ctrl; #$P < 0.05$ and ###$P < 0.001$ vs miR-NC. (E) Venn diagram showing the intersection of miRNAs in SKP-SC-EVs promoting axon regeneration of motor and cortical neurons.
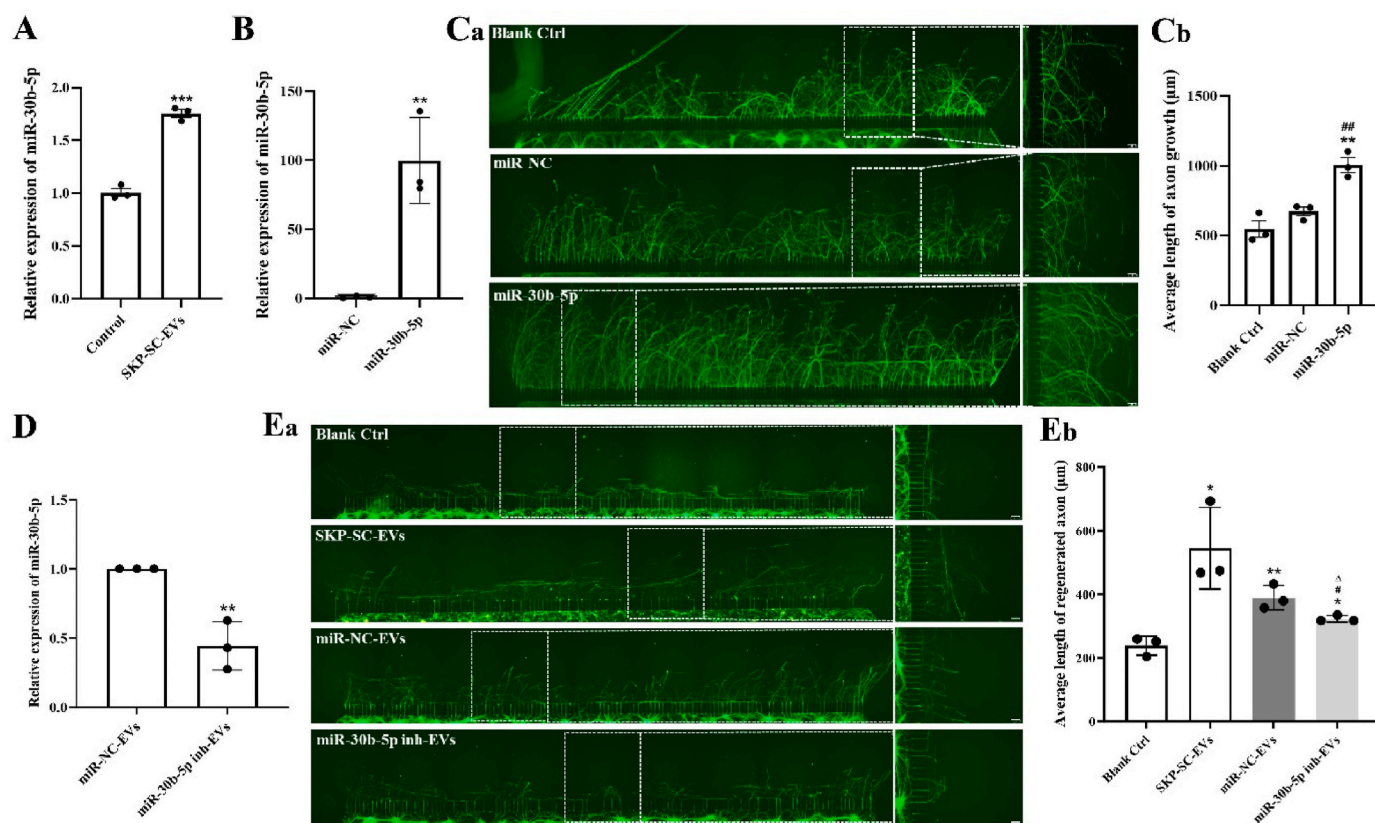
**Fig. 7.** MiR-30b-5p contained in SKP-SC-EVs promoted neuronal axon growth and regeneration. (A) MiR-30b-5p expression in SKP-SC-EVs ($8 \times 10^8$ particles/ml)-treated motor neurons, as detected by qPCR. All data are presented as mean $\pm$ SEM. ***$P < 0.001$ vs Control. (B) The miR-30b-5p overexpression of motor neurons, as detected by qPCR. **$P < 0.01$ vs miR-NC. (C) Immunostaining images (a) of axon growth of motor neurons after miR-30b-5p overexpression in microfluidic devices (scale bar = 100 μm), and histogram (b) comparing the average length of axon growth after miR-30b-5p overexpression. **$P < 0.01$ vs Blank Ctrl; ##$P < 0.01$ vs miR-NC. (D) MiR-30b-5p expression in SKP-SC-EVs transfected with the miR-30b-5p inhibitor, as detected by qPCR. All data are presented as mean $\pm$ SD. **$P < 0.01$ vs miR-NC-EVs. (E) Immunostaining images (a) of axon regeneration of motor neurons after treatment with SKP-SC-EVs transfected with the miR-30b-5p inhibitor in microfluidic devices (scale bar = 100 μm), and histogram (b) comparing the average length of regenerated axons after treatment with SKP-SC-EVs transfected with the miR-30b-5p inhibitor. *$P < 0.05$ and **$P < 0.01$ vs Blank Ctrl; #$P < 0.05$ vs SKP-SC-EVs, △$P < 0.05$ vs miR-NC-EVs.

biocompatibility, and bioaffinity. Our group has already fabricated chitosan-based NGCs, a patented product (No. ZL 0110820.9, China), and achieved considerable success in PNI repair [19]. A NGC with longitudinally oriented physical fillers inserted into the conduit lumen is proven to be more productive at guiding neurite extension and SC migration than a NGC with hollow conduit lumen because physical fillers can form an intraluminal, biomimetic microstructure to reduce random dispersion of regenerating axons inside the NGC [25,26]. PLGA, a common synthetic polymer prepared by the copolymerization of lactide and glycolide in different ratios, exhibits a more appropriate biodegradability than poly (lactic acid) (PLA) with slow degradation or poly (glycolic acid) (PGA) with rapid degradation. Given its favorable biological properties, PLGA fibers are inserted into the lumen of a chitosan conduit to construct a chitosan/PLGA-based NGC capable of absorbing SKP-SC-EVs in a sponge-like manner. In our lab, in-depth studies on chitosan/PLGA-based NGCs have been persistently carried out for decades, involving such aspects as the fabrication process, effectiveness assessment, and safety evaluation [27].

To examine the performance of chitosan/PLGA-based, SKP-SC-EVs-containing TENGs, a 40-mm long sciatic nerve defect in dogs was bridged using 3 different nerve grafts, and their repair outcomes were compared comprehensively and dynamically. A series of evaluations, such as motor function, electrophysiological tests, retrograde tracing, as well as histomorphological assessment and morphometric analysis of both regenerated nerves and target muscles, collectively demonstrated that promotion of sciatic nerve regeneration induced by chitosan/PLGA-based, SKP-SC-EVs-containing TENGs (EV-TENGs) was similar to (and

even slightly better than) that induced by autografts and was significantly superior to that induced by chitosan/PLGA-based TENGs (TENGs). In this study the comparison among different nerve grafts was exmined at 24 weeks post-grafting. Certainly, a longer time period follow up is more informative for performance evaluation of chitosan/PLGA-based, SKP-SC-EVs-containing TENGs (EV-TENGs). In addition, their biosafety and biocompatibility were also examined (data not shown). Since chitosan/PLGA-based NGC was adopted as a template, this study focused on elucidating the significance of incorporation of SKP-SC-EVs into the NGC and further clarifying whether and how this biochemical cue would yield additional positive impacts on PNI repair.

From the perspective of the classification of biochemical cues, EVs are put into the class of bioactive factors derived from support cells. They might function across a species barrier to influence the biological processes of target cells in a variety of ways, e.g., activating cell surface receptors through proteins and bioactive lipid ligands, integrating contents into the plasma membrane of target cells, and transferring biomolecules or organelles to alter cellular states. Concurrently, EV-functionalized biomaterials used to prepare TENGs could provide the optimal physical cues. On the other hand, the use of EVs as biochemical cues instead of support cells represents a favorable way to create a cell-free therapy with more conveniences in the clinic, which may be considered an unique advantage of chitosan/PLGA-based, SKP-SC-EVs-containing TENGs.

Our previous study illustrated that SKP-SC-EVs could modify the microenvironment of peripheral nerve regeneration by delivering non-coding RNA, neurotrophic factors and other bioactive molecules to
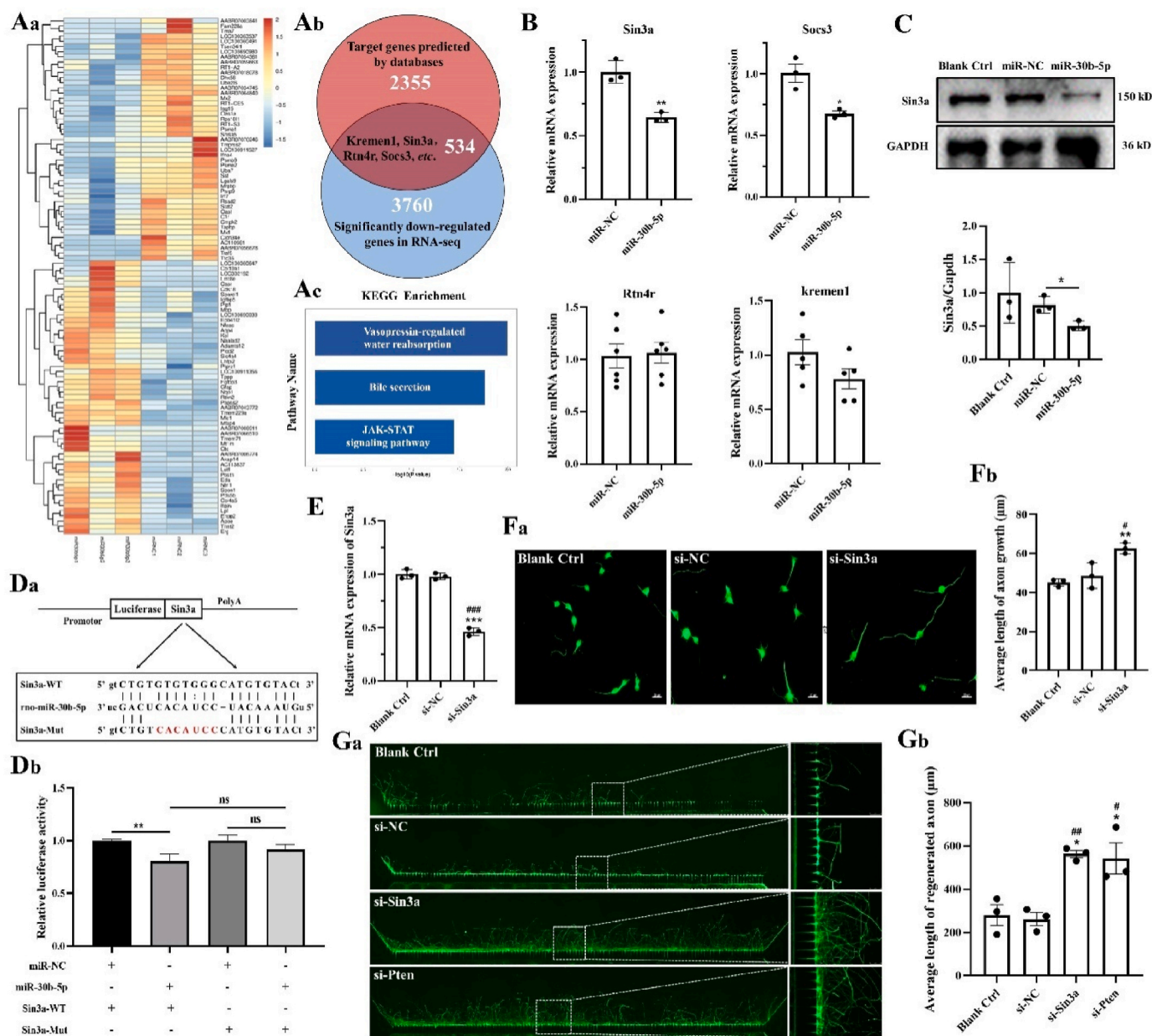
**Fig. 8.** MiR-30b-5p promoted axon regeneration by targeting Sin3a. (**A**) Transcripts heatmap (a) showing the top 100 differential genes in rat motor neurons after miR-30b-5p overexpression, and Venn diagram (b) showing the intersection of database-predicted target genes with genes significantly down-regulated (fold change >1.5) according to transcriptome sequencing. KEGG enrichment analysis (c) of main signaling pathways in which miR-30b-5p was involved. (**B**) Relative mRNA expression of possible target genes after miR-30b-5p overexpression in rat motor neurons. *$P < 0.05$ and **$P < 0.01$ vs miR-NC. (**C**) Histogram comparing the Sin3a protein level of Sin3a after different transfections of rat motor neurons. Representative Western blot images were shown on the top and GAPDH served as a reference gene. *$P < 0.05$ vs miR-NC. (**D**) Construction (a) of luciferase reporter plasmid of Sin3a 3'UTR wild type (WT) and mutant type (Mut) and schematic diagram of binding site to miR-30b-5p. Luciferase activity detection (b) in HEK293T cells co-transfected with miR-30b-5p mimic (or miR-NC) and Sin3a 3'UTR reporter plasmids (WT or Mut). *$P < 0.05$ and ns (no significance) vs miR-NC. (**E**) The interference efficiency of Sin3a in rat motor neurons detected by qPCR. ***$P < 0.001$ vs Blank Ctrl; ###$P < 0.01$ vs si-NC. (**F**) Immunostaining image (a) showing axon growth of rat motor neurons after Sin3a interference. Scale bar = 20 μm. Histogram (b) comparing the average length of axon growth after Sin3a interference. **$P < 0.01$ vs Blank Ctrl; #$P < 0.05$ vs si-NC. (**G**) Immunostaining image (a) showing axon regeneration of rat motor neurons after Sin3a and Pten interference in microfluidic devices. Scale bar = 100 μm. Histogram (b) comparing the average length of regenerated axon after Sin3a and Pten interference. *$P < 0.05$ vs Blank Ctrl; #$P < 0.05$ and ##$P < 0.01$ vs si-NC.

SCs, neurons or other receptor cells [17]. On the other hand, Matrigel effectively mediated the stable release of SKP-SC-EVs *in vitro*; the released SKP-SC-EVs maintained their morphological characteristics and were able to be internalized by nerve cells; even after 28 days of release from the gel, SKP-SC-EVs still exerted the promoting effects on the vitality and growth of nerve cells [17]. Moreover, PKH26-labeled SKP-SC-EVs could be released not only from Matrigel but also from chitosan-based NGCs [18]. These previous findings indicated the

long-lasting biological activity of SKP-SC-EVs *in vitro* and *in vivo*, predicting the feasibility of using chitosan/PLGA-based NGCs as the release carrier of SKP-SC-EVs.

Based on some previous studies [28–30], it can be speculated that SKP-SC-EVs may exert long-term effects through several mechanisms: (1) The membrane proteins and lipid components on the surface of EVs can protect their contents from degradation in the *in vivo* environment, thereby prolonging their half-life. (2) EVs can be endocytosed by
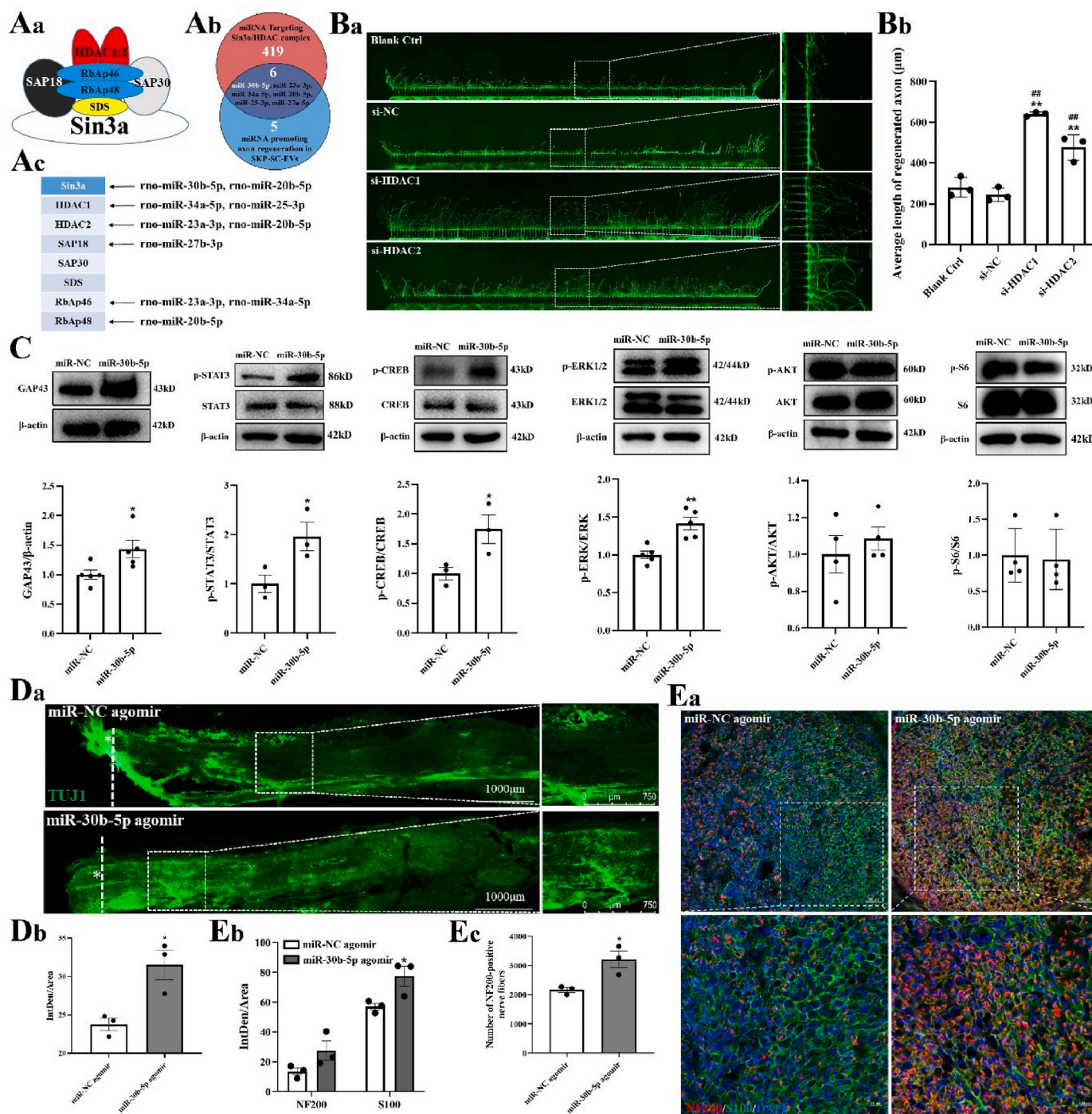
**Fig. 9.** The signaling pathway through which miR-30b-5p-Sin3a/HDAC promoted nerve regeneration. (A) Schematic diagram (a) of Sin3a/HDAC transcriptional repressor complex. Venn diagram (b) showing the intersection of miRNAs targeting the Sin3a/HDAC complex predicted by miRWalk and miRNAs promoting axon regeneration in SKP-SC-EVs. Schematic diagram (c) depicting those miRNAs in SKP-SC-EVs that targeted the Sin3a/HDAC complex and promoted axon regeneration of motor neurons. (B) Immunostaining image (a) showing axon regeneration of motor neurons after HDAC1 and HDAC2 interference in microfluidic devices. Scale bar = 100 μm. Histogram (b) comparing the average length of regenerated axon after HDAC1 and HDAC2 interference. All data are presented as mean ± SEM. **$P$ < 0.01 vs Blank Ctrl; ##$P$ < 0.01 vs si-NC. (C) Histogram comparing the protein levels of GAP43 (n = 5), p-STAT3 (n = 3), p-CREB (n = 3), p-ERK1/2 (n = 5), p-AKT (n = 4) or p-S6 (n = 4) after miR-30b-5p overexpression in motor neurons. *$P$ < 0.05 and **$P$ < 0.01 vs that after transfection with miR-NC. Representative Western blot images were shown on the top where β-actin served as a reference gene. (D) Immunostaining images (a) showing longitudinal sections of rat crushed sciatic nerve after transfection of miR-30b-5p agomir. Scale bar = 1000 μm (left) and 750 μm (right). Histogram (b) comparing the average fluorescence intensity of Tuj1 (green)-labeled regenerating nerves (n = 3). *$P$ < 0.05 vs miR-NC agomir. (E) Immunostaining images (a) showing cross sections of rat crushed sciatic nerve with NF200-stained axons (red), S100-stained myelin sheaths (green), and DAPI-counterstained nucleus (blue) after transfection with miR-30b-5p agomir or miR-NC agomir. Scale bar = 50 μm (upper) and 20 μm (lower). Histogram (b) comparing the average fluorescence intensity of NF200 or S100 in rat crushed sciatic nerves (n = 3) after transfection with miR-30b-5p agomir or miR-NC agomir. Histogram (c) comparing the average number of NF200-positive nerve fibers in rat crushed sciatic nerves (n = 3) after transfection with miR-30b-5p agomir or miR-NC agomir. *$P$ < 0.001 vs miR-NC agomir.

recipient cells and can release their cargo intracellularly to prolong their biological activity. (3) The chitosan/PLGA-based NGC can continuously release EVs for a certain period to prolong the local action time of EVs. (4) EVs can regulate gene expression and signaling pathways in recipient cells through paracrine effects, and this regulatory effect may persist for a certain period, even if the EVs themselves have been degraded. All these findings indicate the persistent biological activity of SKP-SC-EVs.

To better gain mechanistic insight into the promotive effects of SKP-SC-EVs on PNI repair, we analyzed their molecular composition through miRNA sequencing. The top 60 highly expressed miRNAs in SKP-SC-EVs were identified and key biomolecules involved in nerve regeneration were found. Based on existing literature reports, miR-30b-5p, miR-26a-5p, miR-20b-5p, miR-34a-5p, miR-22-3p, and miR-93-5p are involved in neuroinflammation, neuropathic sensitivity and pain progression [31–35]; miR-23a-3p, miR-103-3p, miR-26a-5p, miR-99a-5p, miR-25-3p, miR-29a-3p, miR-27a-5p, miR-222-3p, miR-34a-5p, miR-17-5p, and miR-22-3p play critical roles in the regulation of neural cell survival, proliferation, migration, apoptosis, sensitivity to radiation and chemotherapy, and the secretion of neurotrophic factors [36–42]; miR-26a-5p, miR-29a-3p, miR-204-5p, miR-92a, and miR-17-5p are vital in the processes of neuronal differentiation, neurite development and growth, as well as axonal regeneration and myelination [43–45]. The above-mentioned miRNAs were selected for further validation based on their critical roles in axonal outgrowth and regeneration.

Therefore, a miRNA screening library was established, which revealed that a variety of highly expressed miRNAs in SKP-SC-EVs were associated with axon growth and regeneration of rat motor or cortical neurons. As is known, cortical neurons are usually used for studying central nerve regeneration, especially for mechanism exploration and molecular screening. Considering that peripheral nerve regeneration is a complex biological process involving coordinated regulation of the central and peripheral nervous systems, we select both motor and cortical neurons to unravel the effects of SKP-SC-EVs on neuron regrowth. Notably, miR-30b-5p emerged as an essential player in this process, despite not being the most abundantly expressed miRNA. As an important regulator in the development and disease, the miR-30 family promptly attracted our attention. The family comprises miR-30a, miR-30b, miR-30c-1, miR-30c-2, miR-30d and miR-30e members, and is encoded by 6 genes located on chromosomes 1,6 and 8 [46]. The 6 miRNA members share a common seed sequence at the 5′ end, but have different compensation sequences at the 3′ end, thereby allowing them to target different genes and pathways, and to exert corresponding biological functions [47]. Intriguingly, accumulating evidence suggests that the miR-30 family plays an important regulatory role in the pathogenesis of nervous system-related diseases [48–53]. This study found that the overexpression of miR-30b-5p not only promoted the growth of neuronal axons but also significantly promoted axon regeneration after axon severance. Inhibiting miR-30b-5p in SKP-SC-EVs significantly reduced the promotive effect of SKP-SC-EVs on axon regeneration, indicating that SKP-SC-EVs could promote the growth and regeneration of neuronal axons through miR-30b-5p. After the inhibition of miR-30b-5p, however, SKP-SC-EVs still maintained a certain promotive effect on axon regeneration, suggesting that they might contain other molecules, including miRNAs, nucleic acids and proteins, besides miR-30b-5p to facilitate neuronal growth and regeneration. The specific components and functions still require further in-depth research to elucidate.

Subsequently, the altered gene expressions induced by miR-30b-5p overexpression in motor neurons were analyzed by high-throughput transcriptome sequencing. The target genes of miR-30b-5p were predicted by miRWalk database [54], and 4 genes linked to nerve regeneration were screened from the intersection of downregulated genes and genes in the database indicated by GO annotation analysis. These 4 genes were Kremen1, Sin3a, Rtn4r and Socs3. qPCR examination showed that the mRNA expression levels of Sin3a and Socs3 in motor neurons were significantly altered after miR-30b-5p overexpression. The binding site between miR-30b-5p and the 3′UTR of Sin3a or Socs3 was predicted by the RNAhybrid database.

As previously reported, conditional co-deletion of Pten and Socs3 significantly enhances the early regeneration of DRG axons after sciatic nerve crush injury and induces retinal axon regeneration to form functional synapses in superior colliculus, thus repairing the active synapses of suprachiasmatic neurons [55–57]. It was concluded that Socs3 might exert an inhibitory effect on nerve regeneration in both central and peripheral nervous systems. In contrast, the role of Sin3a in nerve regeneration has yet to be thoroughly studied. According to previous findings in our lab [58], Sin3a and 16 other transcription factors and chromatin regulators affected the progress of myelination; Sin3a silencing inhibited SC migration and differentiation at the promyelination stage and promoted SC proliferation at the immature stage; SC differentiation and maturation were regulated by the synergistic regulation of Sin3a/HDAC2 complex and Sox10. Inspired by these observations, we explored whether and how Sin3a affected axon regeneration. To verify the possibility of Sin3a as a potential target gene of miR-30b-5p, luciferase reporter gene experiments revealed that miR-30b-5p had Sin3a-binding sites, and Sin3a interference significantly promoted axon growth and regeneration of motor neurons after disconnection, indicating that the inhibitory effect of Sin3a was similar to that of Pten. Collectively, all the findings suggested that miR-30b-5p might enhance peripheral nerve regeneration by targeting Sin3a.

The main function of Sin3a in cells is to maintain the stability of the Sin3a/HDAC complex as a scaffold protein. The Sin3a/HDAC complex is an octamer composed of the Sin3a, HDAC1, HDAC2, RBAP46, RBAP48, SAP18, SAP30 and SDS3 subunits, and mainly relies on HDAC1/2 to affect the level of protein acetylation [59]. The miRNAs capable of targeting the Sin3a/HDAC transcriptional repression complex were predicted by miRWalk database, and they were intersected with previously screened miRNAs capable of promoting axon regeneration. We noted that multiple miRNAs in SKP-SC-EVs might directly target various subunits of the Sin3a/HDAC complex. In brief, miR-30b-5p and miR-20-5p might target Sin3a; miR-34a-5p, miR-25-3p, miR-23a-3p and miR-20b-5p might target HDAC1/HDAC2; miR-27b-3p might target SAP18; miR-23a-3p and miR-34a-5p might target RbAp46; miR-20b-5p might target RbAp48. Although the binding sites between these miRNAs and the Sin3a/HDAC complex have not been verified, it was rationally deduced that these miRNAs residing in SKP-SC-EVs played a synergistic role in the promotion of nerve regeneration by targeting the Sin3a/HDAC complex.

Furthermore, KEGG pathway enrichment analysis revealed that the ability of miR-30b-5p to target the Sin3a/HDAC complex might be linked to JAK/STAT3 signaling pathway in that the phosphorylation levels of STAT3, ERK or CREB were significantly increased after miR-30b-5p overexpression. Previous studies have reported the involvement of Sin3a in signaling pathways: Sin3a regulates inflammatory immune response, cell proliferation, differentiation and tissue homeostasis through interaction with STAT3 [60–62]; Sin3a regulates STAT3 transcriptional activity and plays a central role in Th17 cell differentiation in inflammatory diseases and opportunistic infections [63]; ERK is activated in the hippocampus of mice after Sin3a conditional knockout, thereby enhancing the synaptic plasticity of hippocampal neurons [64]. In this way, we assumed that miR-30b-5p contained in SKP-SC-EVs could activate STAT3, ERK and CREB phosphorylation to promote neuronal axon regeneration by targeting Sin3a/HDAC complex. The detailed involvement of signaling pathways in the targeting is worthy to be clarified in future works.

## 5. Conclusion

To summarize, we developed a novel TENG by incorporating SKP-SC-EVs into a chitosan/PLGA-based NGC, and successfully used it for bridging a 40-mm sciatic nerve defect in beagle dogs. This chitosan/

PLGA-based, SKP-SC-EVs-containing TENG significantly accelerated the recovery of hind limb motor and electrophysiological functions, supported the outgrowth and myelination of regenerated axons, and alleviated the denervation-induced atrophy of target muscles. The nerve repair outcome achieved by chitosan/PLGA-based, SKP-SC-EVs-containing TENGs prevailed over that by chitosan/PLGA-based TENGs (chitosan/PLGA-based NGCs alone). SKP-SC-EVs were rich in a variety of miRNAs related to axon growth and regeneration of neurons. MiR-30b-5p was the most important miRNA in SKP-SC-EVs, and promoted nerve regeneration by targeting the Sin3a/HDAC complex and activating the phosphorylation of ERK, STAT3 or CREB. Taken together, all the results indicated that the incorporation of SKP-SC-EVs might be helpful in developing a promising, cell-free configuration of TENGs used for PNI repair.

## Data availability

The data that support the findings of this study are available on request from the corresponding author.

## Ethics approval and consent to participate

All procedures involving experimental animals were conducted according to the institutional guidelines of Animal Care and Use Committee at Nantong University, and approved by the Experimental Animal Administration Committee of Jiangsu Province, China.

## CRediT authorship contribution statement

**Miaomei Yu:** Writing – review & editing, Writing – original draft, Visualization, Methodology, Investigation, Funding acquisition, Data curation. **Mi Shen:** Visualization, Methodology, Data curation, Conceptualization. **Daiyue Chen:** Methodology, Investigation. **Yan Li:** Methodology, Investigation. **Qiang Zhou:** Visualization, Methodology, Investigation. **Chunyan Deng:** Methodology, Investigation. **Xinyang Zhou:** Validation, Formal analysis. **Qi Zhang:** Writing – review & editing, Data curation. **Qianru He:** Methodology, Data curation. **Hongkui Wang:** Methodology, Investigation. **Meng Cong:** Methodology. **Haiyan Shi:** Data curation. **Xiaosong Gu:** Supervision, Project administration. **Songlin Zhou:** Supervision, Funding acquisition, Formal analysis. **Fei Ding:** Supervision, Resources, Project administration, Funding acquisition.

## Declaration of competing interest

The authors declare that they have no known competing financial interests or personal relationships that could have appeared to influence the work reported in this paper.

## Acknowledgements

## Appendix A. Supplementary data

Supplementary data to this article can be found online at https://doi.org/10.1016/j.bioactmat.2024.06.011.

## References

[1] Y. Jiang, X. Tang, T. Li, J. Ling, Y. Yang, The success of biomaterial-based tissue engineering strategies for peripheral nerve regeneration, Front. Bioeng. Biotechnol. 10 (2022) 1039777.

[2] K.A. Sarhane, C. Qiu, T.G.W. Harris, P.J. Hanwright, H.Q. Mao, S.H. Tuffaha, Translational bioengineering strategies for peripheral nerve regeneration: opportunities, challenges, and novel concepts, Neural Regen Res 18 (2023) 1229–1234.

[3] M.J. Carr, A.P. Johnston, Schwann cells as drivers of tissue repair and regeneration, Curr. Opin. Neurobiol. 47 (2017) 52–57.

[4] M. Bosch-Queralt, R. Fledrich, R.M. Stassart, Schwann cell functions in peripheral nerve development and repair, Neurobiol. Dis. 176 (2023) 105952.

[5] S. Yi, Y. Zhang, X. Gu, L. Huang, K. Zhang, T. Qian, X. Gu, Application of stem cells in peripheral nerve regeneration, Burns Trauma 8 (2020) tkaa002.

[6] T. Yu, Y. Xu, M.A. Ahmad, R. Javed, H. Hagiwara, X. Tian, Exosomes as a promising Therapeutic strategy for peripheral nerve injury, Curr. Neuropharmacol. 19 (2021) 2141–2151.

[7] I.A. McKenzie, J. Biernaskie, J.G. Toma, R. Midha, F.D. Miller, Skin-derived precursors generate myelinating Schwann cells for the injured and dysmyelinated nervous system, J. Neurosci. 26 (2006) 6651–6660.

[8] S. Walsh, J. Biernaskie, S.W. Kemp, R. Midha, Supplementation of acellular nerve grafts with skin derived precursor cells promotes peripheral nerve regeneration, Neuroscience 164 (2009) 1097–1107.

[9] H. Wang, J. Wu, X. Zhang, L. Ding, Q. Zeng, Study of synergistic role of allogenic skin-derived precursor differentiated Schwann cells and heregulin-1beta in nerve regeneration with an acellular nerve allograft, Neurochem. Int. 97 (2016) 146–153.

[10] C. Zhu, J. Huang, C. Xue, Y. Wang, S. Wang, S. Bao, R. Chen, Y. Li, Y. Gu, Skin derived precursor Schwann cell-generated acellular matrix modified chitosan/silk scaffolds for bridging rat sciatic nerve gap, Neurosci. Res. 135 (2018) 21–31.

[11] M. Li, X. Cheng, S. Feng, H. Zhu, P. Lu, P. Zhang, X. Cai, P. Qiao, X. Gu, G. Wang, C. Xue, H. Wang, Skin precursor-derived Schwann cells accelerate in vivo prevascularization of tissue-engineered nerves to promote peripheral nerve regeneration, Glia 71 (2023) 1755–1769.

[12] C. Xue, H. Zhu, H. Wang, Y. Wang, X. Xu, S. Zhou, D. Liu, Y. Zhao, T. Qian, Q. Guo, J. He, K. Zhang, L. Gong, J. Yang, S. Yi, B. Yu, Y. Wang, Y. Liu, Y. Yang, F. Ding, X. Gu, Skin derived precursors induced Schwann cells mediated tissue engineering-aided neuroregeneration across sciatic nerve defect, Bioact. Mater. 33 (2024, March) 19.

[13] G. van Niel, G. D'Angelo, G. Raposo, Shedding light on the cell biology of extracellular vesicles, Nat. Rev. Mol. Cell Biol. 19 (2018) 213–228.

[14] H.Y. Kim, S. Kwon, W. Um, S. Shin, C.H. Kim, J.H. Park, B.S. Kim, Functional extracellular vesicles for regenerative medicine, Small 18 (2022) e2106569.

[15] M. Cong, M. Shen, X. Wu, Y. Li, L. Wang, Q. He, H. Shi, F. Ding, Improvement of sensory neuron growth and survival via negatively regulating PTEN by miR-21-5p-contained small extracellular vesicles from skin precursor-derived Schwann cells, Stem Cell Res. Ther. 12 (2021) 80.

[16] X. Wu, L. Wang, M. Cong, M. Shen, Q. He, F. Ding, H. Shi, Extracellular vesicles from skin precursor-derived Schwann cells promote axonal outgrowth and regeneration of motoneurons via Akt/mTOR/p70S6K pathway, Ann. Transl. Med. 8 (2020) 1640.

[17] M. Yu, G. Gu, M. Cong, M. Du, W. Wang, M. Shen, Q. Zhang, H. Shi, X. Gu, F. Ding, Repair of peripheral nerve defects by nerve grafts incorporated with extracellular vesicles from skin-derived precursor Schwann cells, Acta Biomater. 134 (2021) 190–203.

[18] X. Zhou, M. Yu, D. Chen, C. Deng, Q. Zhang, X. Gu, F. Ding, Chitosan nerve grafts incorporated with SKP-SC-EVs induce peripheral nerve regeneration, Tissue Eng Regen Med 20 (2023) 309–322.

[19] X. Wang, W. Hu, Y. Cao, J. Yao, J. Wu, X. Gu, Dog sciatic nerve regeneration across a 30-mm defect bridged by a chitosan/PGA artificial nerve graft, Brain 128 (2005) 1897–1910.

[20] C. Xue, N. Hu, Y. Gu, Y. Yang, Y. Liu, J. Liu, F. Ding, X. Gu, Joint use of a chitosan/PLGA scaffold and MSCs to bridge an extra large gap in dog sciatic nerve, Neurorehabilitation Neural Repair 26 (2012) 96–106.

[21] X. Dong, Y. Yang, Z. Bao, A.C. Midgley, F. Li, S. Dai, Z. Yang, J. Wang, L. Liu, W. Li, Y. Zheng, S. Liu, Y. Liu, W. Yu, J. Liu, M. Fan, M. Zhu, Z. Shen, G. Xiaosong, D. Kong, Micro-nanofiber composite biomimetic conduits promote long-gap peripheral nerve regeneration in canine models, Bioact. Mater. 30 (2023) 98–115.

[22] Q.R. He, M. Cong, F.H. Yu, Y.H. Ji, S. Yu, H.Y. Shi, F. Ding, Peripheral nerve fibroblasts secrete neurotrophic factors to promote axon growth of motoneurons, Neural Regen Res 17 (2022) 1833–1840.

[23] M.K.E. Schafer, I. Tegeder, NG2/CSPG4 and progranulin in the posttraumatic glial scar, Matrix Biol. 68–69 (2018) 571–588.

[24] X. Gu, F. Ding, D.F. Williams, Neural tissue engineering options for peripheral nerve regeneration, Biomaterials 35 (2014) 6143–6156.

[25] Y. Peng, K.Y. Li, Y.F. Chen, X.J. Li, S. Zhu, Z.Y. Zhang, X. Wang, L.N. Duan, Z. J. Luo, J.J. Du, J.C. Wang, Beagle sciatic nerve regeneration across a 30 mm defect bridged by chitosan/PGA artificial nerve grafts, Injury 49 (2018) 1477–1484.

[26] D. Perretta, S. Green, Bridging the gap in peripheral nerve repair, Bull. Hosp. Jt. Dis. 75 (2017) 57–63, 2013.

[27] P. Lu, G. Wang, T. Qian, X. Cai, P. Zhang, M. Li, Y. Shen, C. Xue, H. Wang, The balanced microenvironment regulated by the degradants of appropriate PLGA scaffolds and chitosan conduit promotes peripheral nerve regeneration, Mater Today Bio 12 (2021) 100158.

[28] Y. Wang, P. Li, L. Kong, Chitosan-modified PLGA nanoparticles with versatile surface for improved drug delivery, AAPS PharmSciTech 14 (2013) 585–592.

[29] J. Yu, S. Sane, J.E. Kim, S. Yun, H.J. Kim, K.B. Jo, J.P. Wright, N. Khoshdoozmasouleh, K. Lee, H.T. Oh, K. Thiel, A. Parvin, X. Williams, C. Hannon, H. Lee, D.K. Kim, Biogenesis and delivery of extracellular vesicles: harnessing the power of EVs for diagnostics and therapeutics, Front. Mol. Biosci. 10 (2023) 1330400.

[30] T.B. Gandek, L. van der Koog, A. Nagelkerke, A comparison of cellular uptake mechanisms, delivery efficacy, and intracellular fate between liposomes and extracellular vesicles, Adv. Healthcare Mater. 12 (2023) e2300319.

[31] J. Liao, J. Liu, G. Long, X. Lv, MiR-30b-5p attenuates neuropathic pain by the CYP24A1-Wnt/beta-catenin signaling in CCI rats, Exp. Brain Res. 240 (2022) 263–277.

[32] Y. Lu, J. Zhang, F. Zeng, P. Wang, X. Guo, H. Wang, Z. Qin, T. Tao, Human PMSCs-derived small extracellular vesicles alleviate neuropathic pain through miR-26a-5p/Wnt5a in SNI mice model, J. Neuroinflammation 19 (2022) 221.

[33] H. You, L. Zhang, Z. Chen, W. Liu, H. Wang, H. He, MiR-20b-5p relieves neuropathic pain by targeting Akt3 in a chronic constriction injury rat model, Synapse 73 (2019) e22125.

[34] L. Li, Y. Luo, Y. Zhang, M. Wei, M. Zhang, H. Liu, Z. Su, CircZNF609 aggravates neuropathic pain via miR-22-3p/ENO1 axis in CCI rat models, Gene 763 (2020) 145069.

[35] R. Staal, T. Khayrullina, R. Christensen, S. Hestehave, H. Zhou, M. Cajina, M. E. Nattini, A. Gandhi, S.M. Fallon, M. Schmidt, S.H. Zorn, R.M. Brodbeck, G. Chandrasena, M. Segerdahl, N. Breysse, A.T. Hopper, T. Moller, G. Munro, P2X7 receptor-mediated release of microglial prostanoids and miRNAs correlates with reversal of neuropathic hypersensitivity in rats, Eur. J. Pain 26 (2022) 1304–1321.

[36] H. Zuo, S. Liu, X. Li, G. Hou, miR-23a-3p promotes the development of colon cancer by inhibiting the expression of NDRG4, Clin. Transl. Oncol. 25 (2023) 933–940.

[37] Y. Shen, Z. Cheng, S. Chen, Y. Zhang, Q. Chen, S. Yi, Dysregulated miR-29a-3p/PMP22 modulates Schwann cell proliferation and migration during peripheral nerve regeneration, Mol. Neurobiol. 59 (2022) 1058–1072.

[38] C. Compagnoni, V. Zelli, A. Bianchi, A. Di Marco, R. Capelli, D. Vecchiotti, L. Brandolini, A.M. Cimini, F. Zazzeroni, M. Allegretti, E. Alesse, A. Tessitore, MicroRNAs expression in response to rhNGF in epithelial corneal cells: focus on neurotrophin signaling pathway, Int. J. Mol. Sci. 23 (2022).

[39] X. Xu, R. Gao, S. Li, N. Li, K. Jiang, X. Sun, J. Zhang, Circular RNA circZNF292 regulates H(2) O(2) -induced injury in human lens epithelial HLE-B3 cells depending on the regulation of the miR-222-3p/E2F3 axis, Cell Biol. Int. 45 (2021) 1757–1767.

[40] H. Zhang, X.M. Zhang, D.D. Zong, X.Y. Ji, H. Jiang, F.Z. Zhang, S.D. He, miR-34a-5p up-regulates the IL-1beta/COX2/PGE2 inflammation pathway and induces the release of CGRP via inhibition of SIRT1 in rat trigeminal ganglion neurons, FEBS Open Bio 11 (2021) 300–311.

[41] P. Hong, M. Jiang, H. Li, Functional requirement of dicer1 and miR-17-5p in reactive astrocyte proliferation after spinal cord injury in the mouse, Glia 62 (2014) 2044–2060.

[42] T. Hu, F. Wang, G. Han, LncRNA PSMB8-AS1 acts as ceRNA of miR-22-3p to regulate DDIT4 expression in glioblastoma, Neurosci. Lett. 728 (2020) 134896.

[43] A. Majer, S.J. Medina, Y. Niu, B. Abrenica, K.J. Manguiat, K.L. Frost, C.S. Philipson, D.L. Sorensen, S.A. Booth, Early mechanisms of pathobiology are revealed by transcriptional temporal dynamics in hippocampal CA1 neurons of prion infected mice, PLoS Pathog. 8 (2012) e1003002.

[44] L.N. Su, X.Q. Song, Z.X. Xue, C.Q. Zheng, H.F. Yin, H.P. Wei, Network analysis of microRNAs, transcription factors, and target genes involved in axon regeneration, J. Zhejiang Univ. - Sci. B 19 (2018) 293–304.

[45] B. Mead, E. Cullather, N. Nakaya, Y. Niu, C. Kole, Z. Ahmed, S. Tomarev, Viral delivery of multiple miRNAs promotes retinal ganglion cell survival and functional preservation after optic nerve crush injury, Exp. Eye Res. 197 (2020) 108071.

[46] M. Kumar, G. Li, Emerging role of MicroRNA-30c in neurological disorders, Int. J. Mol. Sci. 24 (2022).

[47] L. Mao, S. Liu, L. Hu, L. Jia, H. Wang, M. Guo, C. Chen, Y. Liu, L. Xu, miR-30 family: a promising regulator in development and disease, BioMed Res. Int. 2018 (2018) 9623412.

[48] X. Fu, Y. Shen, W. Wang, X. Li, MiR-30a-5p ameliorates spinal cord injury-induced inflammatory responses and oxidative stress by targeting Neurod 1 through MAPK/ERK signalling, Clin. Exp. Pharmacol. Physiol. 45 (2018) 68–74.

[49] H. Chan-Juan, L. Sen, A. Li-Qianyu, Y. Jian, Y. Rong-Di, MicroRNA-30b regulates the polarity of retinal ganglion cells by inhibiting semaphorin-3A, Mol. Vis. 25 (2019) 722–730.

[50] R. Frances, J. Mata-Garrido, R. de la Fuente, M. Carcelen, M. Lafarga, M. T. Berciano, R. Garcia, M.A. Hurle, M. Tramullas, Identification of epigenetic interactions between MicroRNA-30c-5p and DNA methyltransferases in neuropathic pain, Int. J. Mol. Sci. 23 (2022).

[51] F. Han, Y. Huo, C.J. Huang, C.L. Chen, J. Ye, MicroRNA-30b promotes axon outgrowth of retinal ganglion cells by inhibiting Semaphorin3A expression, Brain Res. 1611 (2015) 65–73.

[52] M. Tan, L. Shen, L. Hou, Epigenetic modification of BDNF mediates neuropathic pain via miR-30a-3p/EP300 axis in CCI rats, Biosci. Rep. 40 (2020).

[53] S. Yi, Q.H. Wang, L.L. Zhao, J. Qin, Y.X. Wang, B. Yu, S.L. Zhou, miR-30c promotes Schwann cell remyelination following peripheral nerve injury, Neural Regen Res 12 (2017) 1708–1715.

[54] H. Dweep, C. Sticht, P. Pandey, N. Gretz, miRWalk–database: prediction of possible miRNA binding sites by "walking" the genes of three genomes, J. Biomed. Inf. 44 (2011) 839–847.

[55] Z.R. Gallaher, O. Steward, Modest enhancement of sensory axon regeneration in the sciatic nerve with conditional co-deletion of PTEN and SOCS3 in the dorsal root ganglia of adult mice, Exp. Neurol. 303 (2018) 120–133.

[56] F. Bei, H.H.C. Lee, X. Liu, G. Gunner, H. Jin, L. Ma, C. Wang, L. Hou, T.K. Hensch, E. Frank, J.R. Sanes, C. Chen, M. Fagiolini, Z. He, Restoration of visual function by enhancing conduction in regenerated axons, Cell 164 (2016) 219–232.

[57] S. Li, Q. He, H. Wang, X. Tang, K.W. Ho, X. Gao, Q. Zhang, Y. Shen, A. Cheung, F. Wong, Y.H. Wong, N.Y. Ip, L. Jiang, W.H. Yung, K. Liu, Injured adult retinal axons with Pten and Socs3 co-deletion reform active synapses with suprachiasmatic neurons, Neurobiol. Dis. 73 (2015) 366–376.

[58] B. Zhang, W. Su, J. Hu, J. Xu, P. Askar, S. Bao, S. Zhou, G. Chen, Y. Gu, Transcriptome analysis of Schwann cells at various stages of myelination implicates chromatin regulator Sin3A in control of myelination identity, Neurosci. Bull. 38 (2022) 720–740.

[59] A. Saunders, X. Huang, M. Fidalgo, M.H. Reimer Jr., F. Faiola, J. Ding, C. Sanchez-Priego, D. Guallar, C. Saenz, D. Li, J. Wang, The SIN3A/HDAC corepressor complex functionally cooperates with NANOG to promote pluripotency, Cell Rep. 18 (2017) 1713–1726.

[60] E. Monteleone, V. Poli, Where Sin3a meets STAT3: balancing STAT3-mediated transcriptional activation and repression, Cancer Res. 79 (2019) 3031–3033.

[61] P.Y. Cheng, Y.P. Lin, Y.L. Chen, Y.C. Lee, C.C. Tai, Y.T. Wang, Y.J. Chen, C.F. Kao, J. Yu, Interplay between SIN3A and STAT3 mediates chromatin conformational changes and GFAP expression during cellular differentiation, PLoS One 6 (2011) e22018.

[62] L. Icardi, R. Mori, V. Gesellchen, S. Eyckerman, L. De Cauwer, J. Verhelst, K. Vercauteren, X. Saelens, P. Meuleman, G. Leroux-Roels, K. De Bosscher, M. Boutros, J. Tavernier, The Sin3a repressor complex is a master regulator of STAT transcriptional activity, Proc. Natl. Acad. Sci. U. S. A. 109 (2012) 12058–12063.

[63] L. Perucho, L. Icardi, E. Di Simone, V. Basso, A. Agresti, A. Vilas Zornoza, T. Lozano, F. Prosper, J.J. Lasarte, A. Mondino, The transcriptional regulator Sin3A balances IL-17A and Foxp3 expression in primary CD4 T cells, EMBO Rep. 24 (2023) e55326.

[64] M. Bridi, H. Schoch, C. Florian, S.G. Poplawski, A. Banerjee, J.D. Hawk, G. S. Porcari, C. Lejards, C.G. Hahn, K.P. Giese, R. Havekes, N. Spruston, T. Abel, Transcriptional corepressor SIN3A regulates hippocampal synaptic plasticity via Homer1/mGluR5 signaling, JCI Insight 5 (2020).